



HELSINKI UNIVERSITY OF TECHNOLOGY
Department of Engineering
Physics and Mathematics

Linda Henriksson

Topographical and Quantitative Characterization of
Visual Field Representation in Human Cortex with
Multifocal fMRI

TEKNILLINEN KORKEAKOULU
TEKNILLISEN FYSIIKAN KIRJASTO
PL 2200 (OTAKAARI 3 A)
02015 TKK

Master's thesis submitted in partial fulfillment of the requirements for the degree
of Master of Science in Technology

Espoo, 15.8.2004

Supervisor: Professor Toivo Katila
Instructor: MD PhD Simo Vanni

Author:	Linda Henriksson
Department:	Department of Engineering Physics and Mathematics
Major subject:	Biomedical Engineering
Minor subject:	Neurobiology
Title:	Topographical and Quantitative Characterization of Visual Field Representation in Human Cortex with Multifocal fMRI
Title in Finnish:	Näkökenttäedustuksen topografinen ja kvantitatiivinen karakterisointi ihmisen aivokuorella multifokaalisen fMRI:n avulla
Chair:	Tfy-99, Biomedical Engineering
Supervisor:	Professor Toivo Katila
Instructor:	MD PhD Simo Vanni
<p>With multifocal technique, responses from several visual field or retinal locations are characterized concurrently. Multifocal technique is used in electroretinograms and visually evoked potentials. In this thesis, multifocal fMRI (mffMRI) and tools for multifocal data analysis have been developed. In addition, human cortex has been analyzed with mffMRI</p> <p>Several visual cortical areas are organized retinotopically, i.e. neighboring locations in visual field are mapped next to each other also in the cortex. Thus far, the retinotopic organization of visual cortex has been mapped in fMRI with so-called phase-encoded approach where the borders between visual areas can be mapped accurately with Fourier analysis. MffMRI responses are discrete, so compared to the phase-encoded response, the data-analysis is more straightforward and visual field representation is accurate also within visual areas.</p> <p>With our multifocal stimulus, visual field ($1^\circ - 12^\circ$) was divided into 60 regions. Six subjects participated in the study. As reference, retinotopy was also mapped with phase-encoded approach. The results from mffMRI are promising; for all the subjects all 60 visual field regions evoked strong responses in V1 and a subset also in V2 and V3. The statistical analysis of multifocal data was done with SPM2 Matlab toolbox and surface-oriented analysis with BALC toolbox. To illustrate the anisotropies in the visual cortex, an mffMRI grid was implemented. In addition, a function for the visualization of the retinotopic organization over an anatomical image has been developed and individual visual field representation in the cortex has been analysed with a mathematical model.</p> <p>MffMRI has potential for wide use in basic research and as clinical tool. One future aim is to develop multifocal MEG paradigm and to use mffMRI results as a priori models in MEG-analysis. For clinical use, it is essential that the statistical analysis of multifocal data has been automated. MffMRI provides rapid and accurate, e.g. preoperative, localization of V1, and objective perimetry to detect small lesions in retinocortical pathway. In addition, plastic changes of visual cortex could be followed with mffMRI.</p>	
Number of Pages: 67	Keywords: Multifocal, fMRI, Visual cortex, Retinotopy
Department fills Approved: _____ Library code: _____	

Tekijä:	Linda Henriksson
Osasto:	Teknillisen fysiikan ja matematiikan osasto
Pääaine:	Lääketieteellinen tekniikka
Sivuaine:	Neurobiologia
Työn nimi:	Näkökenttäedustuksen topografinen ja kvantitatiivinen karakterisointi ihmisen aivokuorella multifokaalisen fMRI:n avulla
Title in English:	Topographical and Quantitative Characterization of Visual Field Representation in Human Cortex with Multifocal fMRI
Professuurin koodi ja nimi:	Tfy-99, Lääketieteellinen tekniikka
Työn valvoja:	Professori Toivo Katila
Työn ohjaaja:	LT Simo Vanni
<p>Multifokaalisella tekniikalla kartoitetaan samanaikaisesti useiden näkökentän tai retinan alueiden vasteita. Multifokaalista tekniikkaa on käytetty elektretinogrammeissa ja näköherätepotentiaaleissa. Tässä työssä on kehitetty multifokaalista fMRI:ta (mffMRI) ja työkaluja multifokaalidatan analysointiin sekä analysoitu näkökentän edustusta ihmisen aivokuorella.</p> <p>Useat aivojen näköalueet ovat järjestyneet retinotooppisesti, eli viereiset näkökentän pisteet kuvautuvat viereisiksi myös aivokuorella. Tähän saakka näköaivokuoren retinotopiaa on fMRI:ssa kartoitettu niin kutsutulla vaihekoodatulla menetelmällä, jossa Fourier-analyysin avulla saadaan tarkasti selvitettyä retinotooppisten näköalueiden rajat. MffMRI:n vasteet ovat erillisiä, joten verrattuna vaihekoodattuun vasteeseen data-analyysi on suoraviivaisempaa ja tieto näkökenttäedustuksesta on tarkkaa myös näköalueiden sisällä.</p> <p>Multifokaaliärsykkeemme sisälsi 60 aluetta eksentrisyyksillä $1^{\circ} - 12^{\circ}$. Tutkimukseen osallistui kuusi koehenkilöä. Vertailun vuoksi retinotopia kartoitettiin myös vaihekoodatulla menetelmällä. MffMRI:n tulokset ovat lupaavia; kaikille koehenkilöille kaikki 60 näkökentän aluetta herättivät voimakkaat vasteet ensimmäisellä näköaivokuorella ja osa lisäksi näköalueilla V2 ja V3. Multifokaalidatalle tehtiin statistinen analyysi SPM2-ohjelmistolla ja pintaorientoitunut analyysi BALC-ohjelmistolla. Näköaivokuoren anisotropian havainnollistamiseksi kehitettiin mffMRI-verkko. Lisäksi on kehitetty funktio, jonka avulla retinotooppista järjestäytymistä voidaan tarkastella myös suoraan anatomisen MRI-kuvan päällä sekä analysoitu näkökentän edustusta yksilötasolla matemaattisella mallilla.</p> <p>MffMRI:lla on potentiaalia laajaan käyttöön perustutkimuksessa ja kliinisenä työkaluna. Tulevaisuudessa on tarkoitus kehittää multifokaalinen MEG-paradigma ja käyttää mffMRI-tuloksia a priori -malleina MEG-analyysissä. Kliiniselle käytölle on olennaista, että multifokaalidatan statistinen analyysi on automatisoitu. MffMRI:n avulla voidaan paikantaa, esimerkiksi ennen leikkausta, tarkasti ja nopeasti ensimmäinen näköaivokuori sekä tutkia yksityiskohtaisesti verkkokalvolta aivokuorelle johtavan hermojärjestelmän eheyttä. Lisäksi mffMRI:n avulla voitaisiin seurata näköaivokuoren plastisia muutoksia.</p>	
Sivumäärä: 67	Avainsanat: Multifokaalinen, fMRI, Näköaivokuori, Retinotopia
<p>Täytetään osastolla</p> <p>Hyväksytty: Kirjasto:</p>	

Preface

This work was carried out in the Brain Research Unit (BRU) of Low Temperature Laboratory and in the Advanced Magnetic Imaging (AMI) Centre in Helsinki University of Technology. I wish to express my gratitude to Academy Professor Riitta Hari for the resources and inspiring working conditions. I would like to thank the instructor of my Master's thesis MD PhD Simo Vanni for his guidance, advice and motivation. PhD Andrew James from Australian National University (Canberra, Australia) I would like to thank for collaboration. James has developed the pattern-pulse multifocal VEP and now made the multifocal stimuli to our fMRI study. In addition, I wish to thank the supervisor of this thesis Professor Toivo Katila for the valuable comments on the text.

I have enjoyed my work in BRU and AMI Centre. I wish to thank all my co-workers, especially Marita Kattelus for help in the measurements, Linda Stenbacka for segmentations of the anatomical data, Antti Tarkiainen for the system support and Ville Renvall for review of the text about MRI and fMRI. In addition, I want to thank all the subjects who participated this study.

My parents and Niksu, my fourteen years old Norwich Terrier, I would like to thank for my happy life and for the encouragement during my studies. My friends, you are all important to me, thanks for being there. Finally, I want to thank Matti for all his help, support and love.

In Espoo, August 15th, 2004

Linda Henriksson

Contents

Preface	ii
List of Abbreviations	v
1 Introduction	1
2 Visual Cortex	3
2.1 On Organization of Primate Visual Cortex	3
2.2 Retinotopy	6
2.3 Human Low Order Visual Areas	7
2.4 Cortical Magnification	9
3 Principles of Magnetic Resonance Imaging	12
3.1 Nuclear Magnetic Resonance	12
3.2 Origin of MR Signal	13
3.3 Imaging Principles	14
3.4 MR Image Contrast	17
3.5 Basic Imaging Sequences	18
4 Functional Magnetic Resonance Imaging	21
4.1 Physiological Changes in Brain During Neural Activation	21
4.2 Blood Oxygenation Level Dependent Signal	22
4.3 Experimental Design	22
5 Phase Encoding Retinotopic Approach and Multifocal fMRI	25
5.1 Phase-Encoded Retinotopic Mapping	25
5.2 Background of Multifocal Method	27
5.3 Multifocal fMRI	29
6 Materials and Methods	31
6.1 Stimulus and Subjects	31
6.2 Data Acquisition	33

6.3	Preprocessing of Data	34
6.4	Statistical Analysis of Functional Data	34
6.5	Surface Oriented Analysis	38
7	Results	40
7.1	Statistical Results of Multifocal Data	40
7.2	Surface Oriented Results	40
7.3	MffMRI Grid on Reconstructed Surface	41
7.4	Application of Log Map Model to mffMRI Data	47
7.5	Localization of V1	49
7.6	Reproducibility of Measurements	50
8	Discussion	51
8.1	On Results	51
8.2	Applications in Basic Research	53
8.3	Applications in Clinical Medicine	53
8.4	Limitations of mffMRI	54
8.5	Conclusions and Future Development	54
	References	55
A	Implementations	62
A.1	MffMRI Grid	62
A.2	3D Display for Multifocal Responses	64
A.3	Estimation of Parameters in Log Polar Map Model of Visual Field Representation in Visual Cortex	65

List of Abbreviations

2D	Two-dimensional
3D	Three-dimensional
BALC	Brain à la Carte
BOLD	Blood oxygenation level dependent
EEG	Electroencephalography
EPI	Echo-planar imaging
ERG	Electroretinogram
FDR	False discovery rate
fMRI	Functional magnetic resonance imaging
FWE	Family-wise error
GLM	General linear model
GRE	Gradient echo
GRF	Gaussian random field theory
LGN	Lateral geniculate nucleus
MEG	Magnetoencephalography
mffMRI	Multifocal functional magnetic resonance imaging
MR	Magnetic resonance
MRI	Magnetic resonance imaging
NMR	Nuclear magnetic resonance
SE	Spin echo
SPM	Statistical parametric mapping
TE	Echo time
TR	Repetition time
V1	Visual area 1, primary visual cortex
V2	Visual area 2
V2d	Dorsal division of V2
V2v	Ventral division of V2
V3	Visual area 3
V5/MT	Visual area 5 / middle temporal area
VEP	Visually evoked potential
VP	Ventral posterior area

Chapter 1

Introduction

The human visual system has been intensively studied since the development of modern neuroimaging methods from 1990s onwards. With multifocal stimulation method, responses from several visual field locations can be mapped concurrently. Sutter [1] introduced the multifocal m-sequence technique, first used in electroretinograms, but it has also been successfully adopted to studies of visually evoked potentials (VEP). James [2] has developed pattern-pulse multifocal VEP, where visual field regions are stimulated in parallel with pulses of pattern contrast. With pattern-pulse stimulation, the response amplitudes are 15 times larger than with conventional pattern reversal stimulation. Both the multifocal electroretinograms and VEPs have established an important role in basic research and as clinical tools.

Thus far, functional magnetic resonance (fMRI) retinotopic mapping has been done with so-called phase-encoded visual stimuli [3]. These stimuli map the polar angle and eccentricity of the visual field by producing a wavelike progressing blood oxygenation level dependent signal. Visual field representation is analyzed by means of Fourier analysis and presented as phase responses on the segmented and reconstructed cortical surface.

The aim of this study has been to develop visual multifocal technique for fMRI. Whereas phase-encoded retinotopic mapping requires Fourier analysis and includes inaccuracies in local phase estimates, with multifocal fMRI (mffMRI) more detailed information on multiple local visual field representations in the visual cortex can be mapped rapidly, and analyzed with common statistical fMRI methods in a more straightforward manner. MffMRI is a novel method for retinotopic mapping and for accurate localization of visual cortical areas.

In this thesis, the results are presented from six subjects who participated the mffMRI experiment. The visual field representation in the cortex is studied with the discrete multifocal responses. Using surface oriented analysis the multifocal results are compared to the retinotopic information obtained with phase-encoded retinotopic mapping. To visualize the multifocal responses in the unfolded cortex simultaneously, an mffMRI grid is implemented. From these data, the relative strength and position of responses can be followed, for example, to study plastic changes in the cortex. The local responses, with known positions and orientations, can be used in further MEG/EEG experiments as strong constraints for source models. Due to discrete local responses in mffMRI, individual magnification factor can be estimated using existing models of human magnification factor. In addition, a 3D display for the multifocal results is developed based on existing tools. The 3D analysis of the mffMRI data can be fully automated which is important for the potential clinical use.

Chapter 2

Visual Cortex

2.1 On Organization of Primate Visual Cortex

Visual information processing in the human visual system begins in photoreceptors in retina. There are two types of photoreceptors, rods and cones, that react differently to light. Rods are very sensitive to light and have only one photopigment, whereas cones are less sensitive to light but have high spatial resolution and the three subgroups of cones are all sensitive to different wavelengths of light. From photoreceptors the visual information is conveyed through horizontal and bipolar cells to retinal ganglion cells. [4]

At the center of the visual field is fovea, the visual field providing the most acute vision. The cone density is much higher in fovea than in more peripheral retinal locations [5]. In addition, the cell density of the retinal ganglion cells is high in the fovea and decreases as function of eccentricity.

The ganglion cell axons form optic nerve, which crosses partially in the optic chiasm. After the chiasm the axons form optic tract, along which visual information is routed to lateral geniculate nucleus (LGN) of thalamus. From the LGN, visual information is projected to visual area 1 (V1) along the so-called optic radiation (see Fig. 2.1). [4]

In the visual system, the receptive field of a neuron is the visual field region whose stimulation the neuron responds. For retinal ganglion cells and neurons in LGN the shape of the receptive field is circular. Retinal ganglion cells can be divided into on-center and off-center ganglion cells. On-center ganglion cell responds heavily when a light spot is turned on in the center of its receptive field and off-center

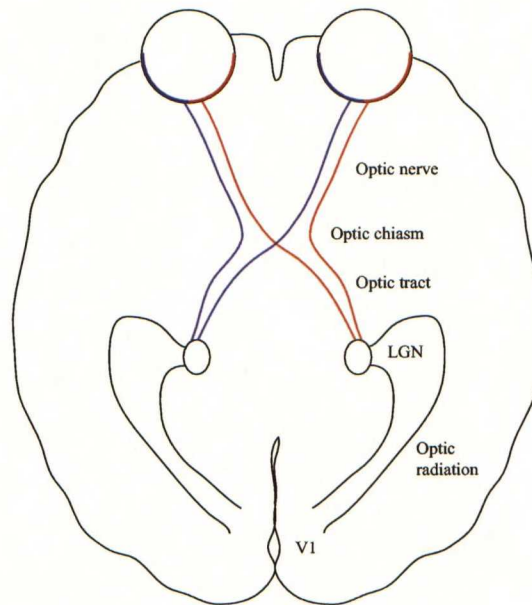


Figure 2.1: *Central visual pathway. Retinal ganglion cell axons form optic nerve. At the optic chiasm axons from the nasal retinas cross. After chiasm, visual information is conveyed along optic tract, which terminates in LGN. From LGN visual information is routed to V1 along optic radiation.*

ganglion cell when the light is turned off. [4]

There are three main types of retinal ganglion cells, M, P and K cells [6]. In the LGN there are two magnocellular layers and four parvocellular layers each of which receives input only from one eye. M cells terminate in the magnocellular layers and P cells in parvocellular layers of the LGN. The main afferent pathways that convey visual information from retina to cortex are called magnocellular (M) stream and parvocellular (P) stream. The neurons in these streams have different response properties. The M neurons are more selective to contrast differences and motion, whereas P neurons have higher color selectivity and process spatial details [7].

Based on the shape of the receptive field, V1 neurons can be divided into simple and complex cells. Like retinal ganglion cells, V1 simple cells have on- and off-responses, but the receptive field is bar-shaped and the cells are sensitive to the length of a bar-shaped moving light. V1 complex cells are sensitive to the orientation of a boundary between light and shadow and direction of moving light source. A complex cell does not respond when its whole receptive field is illuminated, but does respond when a light passes to its receptive field in proper orientation. [4]

V1 neurons are organized into columns perpendicular to cortical surface. In one column, the orientation preference is the same for all the neurons. To the neighboring column, the orientation preference is slightly different. Neighboring columns form a continuous map of orientation preferences. V1 can also be divided into ocular dominance columns, based on which eye dominates in the column. In addition, V1 is organized retinotopically, i.e. neighboring locations in the visual field are mapped next to each other also in the cortex. Retinotopic organization is discussed in more detail in the next section. [4]

Animal studies on monkeys and cats, as well as studies of humans with lesions and functional imaging studies have offered important information on the organization and connectivity of human visual cortical areas. The visual cortex of macaque monkey is the most commonly used model of human visual system, because the visual performances of this monkey and human species are comparable not only psychophysically, but also the functional anatomy appears roughly similar [8]. In macaques, 25 cortical areas respond only to visual stimuli, and another 7 areas can be driven polymodally [9]. The cortical area devoted to vision is large, visual areas occupying approximately 55 % of the macaque neocortex. Nine of the cortical visual areas are in the occipital lobe, of which the largest areas, the visual areas V1 and V2, occupy approximately 11-12 %. In humans, cortical areas responding predominantly to visual stimuli occupy approximately one third of the cerebral cortex [10].

A hierarchical organization of visual areas was revealed in macaques when the main connections between visual cortical areas were identified by their connectivity, cytoarchitectonics, topographic organization and functional characteristics [9]. The development of neuroimaging methods approximately from 1990 onwards have enabled functional studies of the cortical organization in humans. In monkeys, direct recordings from cortical neurons have showed that the timing of activations in different cortical areas does not follow directly the anatomical hierarchy of connections [11]. In addition, visual information from real noisy surroundings can not be resolved with pure feedforward connections of the hierarchical model. Instead, feedback information from higher-order visual areas is necessary to resolve ambiguity in early processing [12].

It is common to divide the visual information processing into ventral and dorsal streams. The visual areas in the ventral pathway are mainly involved in perception and recognition of visual objects, including faces (for a review see [13]). In humans, the object-selective areas in the lateral part of the occipital lobe (e.g. lateral occipital complex LOC) and in the ventral occipito-temporal regions (e.g. fusiform face area FA, parahippocampal place area PA) are intensively studied. The activity of these areas is highly correlated with recognition of the shape of an object rather

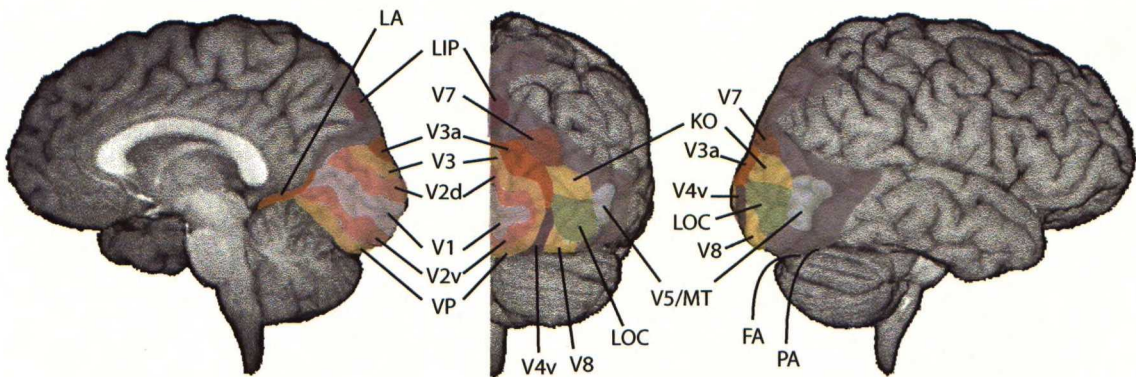


Figure 2.2: *Human visual cortical areas* ($V1$ = visual area 1, $V2d$ = dorsal division of visual area 2, $V2v$ = ventral division of visual area 2, $V3$ = visual area 3, VP = ventral posterior area, $V4v$ = ventral visual area 4, $V7$ = visual area 7, $V8$ = visual area 8, $V5/MT$ = visual area 5 / middle temporal area, KO = kinetic occipital area, LOC = lateral occipital complex, FA = fusiform face area, PA = parahippocampal place area, LIP = lateral intraparietal area, LA = luminance-sensitive area). Adapted from Vanni 2004 [16].

than with more simple visual stimuli like contours.

The dorsal stream is involved in space perception and in combining visual information to motor actions (for a review see [14]). In the dorsal stream, visual information is transferred from $V1$ and $V2$ to visual areas in the superior occipital lobe and parietal lobe. The characteristics of the visual information is transformed to action design, like how to reach an object. A special feature of the visual areas of dorsal stream is that many of these areas are active very rapidly after or even in the same time as $V1$.

In $V1$, and also in higher areas, the cortical neurons innervated by the M stream are activated earlier than those neurons innervated by the P stream [7]. Presumably, the ventral and dorsal streams are not independent but the earlier activated dorsal stream modulates the information processing in the ventral stream [14, 15]. In Fig. 2.2 is shown the structural organization of the main human visual areas.

2.2 Retinotopy

Visual field can be divided into quadrants with vertical and horizontal meridians. Corresponding to visual field, in the intersection point of these meridians in the retina is fovea. Optics of the eye invert and left-right reverse the image onto the

retinal surface. The axons of nasal retinal ganglion cells cross in the optic chiasm, and therefore information from the right half of the visual field is passed to the left hemisphere and vice versa. The axons terminate in topographical order to lateral geniculate nucleus of thalamus. This orderly map of the contralateral hemifield is maintained in projection to primary visual cortex. Hence, the receptive fields of V1 neurons form a continuous topological map of visual field at cortical surface. Fovea is represented posteriorly, usually in the occipital pole, and periphery of the visual field more anteriorly. In V1, horizontal meridian runs approximately along the base of the calcarine sulcus and vertical meridian along the borders of V1. The receptive field size is smallest in V1 neurons and increases in neurons in other visual areas the scaling roughly following the anatomical hierarchy. In addition, receptive fields in V1 and other retinotopic areas are smallest at fovea, and grow approximately linearly with eccentricity. [17]

2.3 Human Low Order Visual Areas

The development of fMRI has enabled noninvasive studies of the organization of the human cortical areas with good spatial resolution. In early studies, the retinotopic organization and borders between human visual cortical areas V1, V2, VP, V3, V3A and V4v were mapped [18]. Already the initial findings revealed that the retinotopic organization of the visual areas is highly consistent among subjects, but there is important individual variability in the visual area boundaries and in the gyral landmarks [19].

Between the macaque and human visual areas there are similarities, but also numerous differences. In humans, the relative sizes of ventral V3 (V3v or VP), dorsal V3 (V3d) and V3A, compared to areas V1 and V2, are significantly greater [10]. In the human brain, the visual areas are withdrawn relatively backwards, compared to macaque brain. There are differences in the geographic locations of the visual areas between human and macaque brains, but the functions of visual areas also differ [10, 8]. In some extent, the visual information processing differs from retinal levels to higher-order signal processing in the temporal and parietal lobes [21]. At least it has been reported that the anatomy and the function of elements of the dorsal stream differ between macaques and humans, suggesting different motion processing.

Visual perception depends much on the signal transfer from V1 to ventral visual areas [22]; hence patients with lesion in V1 usually are perceptually blind. However, V1 cells are sensitive to local features, whereas global features must be detected by cells with larger receptive fields [12]. The architectonic boundary of

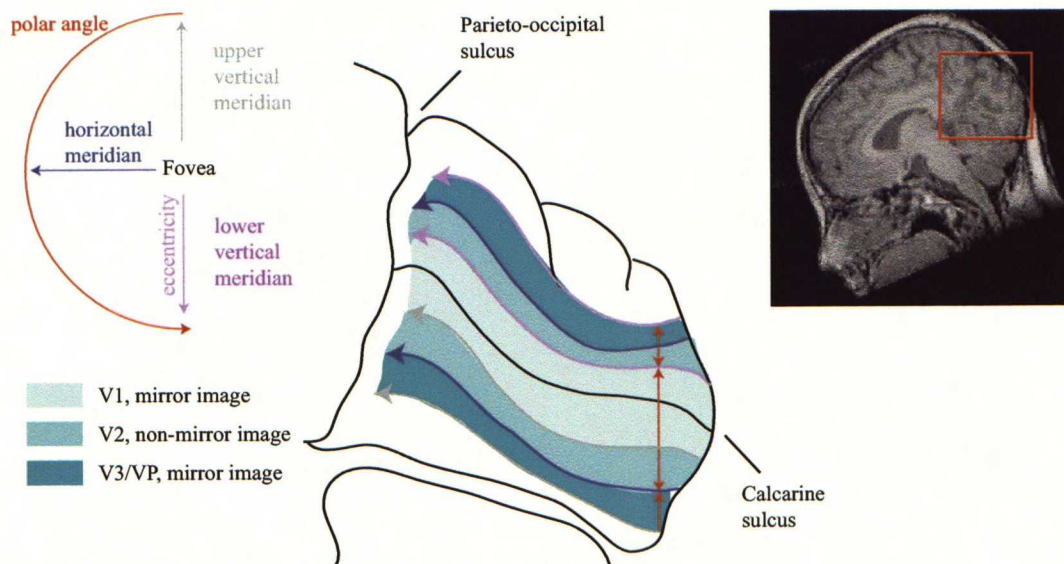


Figure 2.3: A schematic diagram of retinotopic organization in visual areas V1, V2 and V3/VP. In V1, the retinotopic organization is mirror symmetric, so upper visual field is represented below and lower visual field above calcarine sulcus. Upper vertical meridian is represented between V1 and ventral V2. Lower vertical meridian is represented between V1 and dorsal V2 and horizontal meridian between V2 and V3/VP. In V2, the retinotopic organization is nonmirror symmetric and in V3/VP again mirror symmetric. Fovea is represented in the occipital pole and peripheral parts of the visual field near parieto-occipital sulcus. Modified from Engel et al. 1997 [20].

V1 has been identified to run near the borders of the calcarine sulcus, but there are significant differences between individuals [10]. Next to V1 is V2, which forms a long belt along most of the border of V1 [12]. In macaques, V2 is characterized by alternating light and dark cytochrome oxidase stripes perpendicular to V1/V2 border [23]. The current view is that color, form and depth information is separately processed in these thin, pale and thick stripes, correspondingly [23]. It has been proposed that the identification of visual borders and surfaces originates in V1 and continues in V2, where through feedback connections V2 is involved in capturing objects from the background [23].

In monkeys, V3 neurons are more selective to orientation, motion and depth than V1 and V2 neurons. Neurons in human V5 are more sensitive to the movement and direction of the visual stimuli than neurons in other visual areas [12]. The role of human V4v as well as of most of the human visual areas is still much unresolved.

All human low-order visual areas (V1, V2, V3, V3A, V4v and V5) are retino-

topically organized [12]. The regions can be identified from the differences in retinotopic maps. The retinotopic organization can be either mirror or nonmirror symmetric and this symmetry is reversed from one area to the neighboring area [24]. The borders between the areas are either at the horizontal or at the vertical meridian (see Fig. 2.3) [9, 19]. In V1 the retinotopic representation is mirror symmetric. So, upper vertical meridian of the visual field is represented between areas V1 and ventral V2 and lower vertical meridian between V1 and dorsal V2. The horizontal meridian is represented between areas V2 and V3 and vertical meridian again between areas V3 and V3A as well as between areas V3 and V4v [10].

2.4 Cortical Magnification

The cortical surface in V1 devoted to central vision is much larger than the area devoted to representation of an equal sized more peripheral part in the visual field [17]. The expanded representation of fovea can be expressed with cortical magnification which is a function describing how a degree of visual field in different eccentricities is represented in millimeters of cortex. This concept of linear magnification factor was introduced by Daniel and Whitteridge [25]. The cortical magnification has been carefully studied in monkeys with microelectrode recordings and radioactive labeled glucose studies. With macaque monkeys it has been reported that 70% of the total V1 surface represent the central 15° of the visual field.

It has been of interest to construct a mathematical model to the visual field representation in visual cortex based on anatomical and functional findings. The first estimates of cortical magnification in humans were based on comparisons between visual field deficits and lesions in V1. These measures underestimated the magnification of central vision. fMRI has enabled the study of human cortical magnification in healthy brain with a good spatial resolution [18, 26]. fMRI studies [20, 24, 26] have suggested the following equations for the inverse of human cortical magnification M

$$1/M = E/15.87 \quad (2.1)$$

$$1/M = (E + 0.08)^{1.26}/20.05 \quad (2.2)$$

$$1/M = 0.065E + 0.054, \quad (2.3)$$

where E is eccentricity from fovea.

A conformal mapping technique has been introduced for the topographic visual field representation of V1 by Schwartz [27, 28]. With conformal mapping the two-dimensional visual space is mapped to the two-dimensional unfolded cortical surface (see Fig. 2.4). A point in the visual space $z = \phi \exp(i\theta)$ (ϕ eccentricity, θ polar angle) is mapped to a point w in the unfolded cortex

$$w = k \cdot \ln(z + a), \quad (2.4)$$

where both w and z are complex numbers, a is a scalar constant reflecting the proportion of V1 devoted to foveal representation and k is an overall scaling factor. For small z (i.e. $z \ll a$)

$$\ln(z + a) \simeq \ln(a) + \frac{z}{a}, \quad (2.5)$$

the cortical map function is essentially linear and the magnification factor constant. When $z \gg a$, the mapping function is approximately logarithmic,

$$\ln(z + a) \simeq \ln(z). \quad (2.6)$$

The cortical magnification factor is the magnitude of the derivative of this cortical map function

$$M_{Cortex} = |w'| = \left| \frac{k}{z + a} \right|. \quad (2.7)$$

The shape of unfolded V1 is approximately an ellipse [28]. Thus, the simple complex logarithmic fit (2.4) begins to fail around eccentricities of 15-20°. A two-parametric mapping method has been proposed to map the full-field topography of V1

$$w = k \cdot \ln \left(\frac{z + a}{z + b} \right), \quad (2.8)$$

where a and b are scalar constants [28].

The use of conformal mapping and complex function in the model of retinotopic organization implies that this mapping of visual field is isotropic, i.e. independent of direction. That is, magnification depends only on distance from fovea.

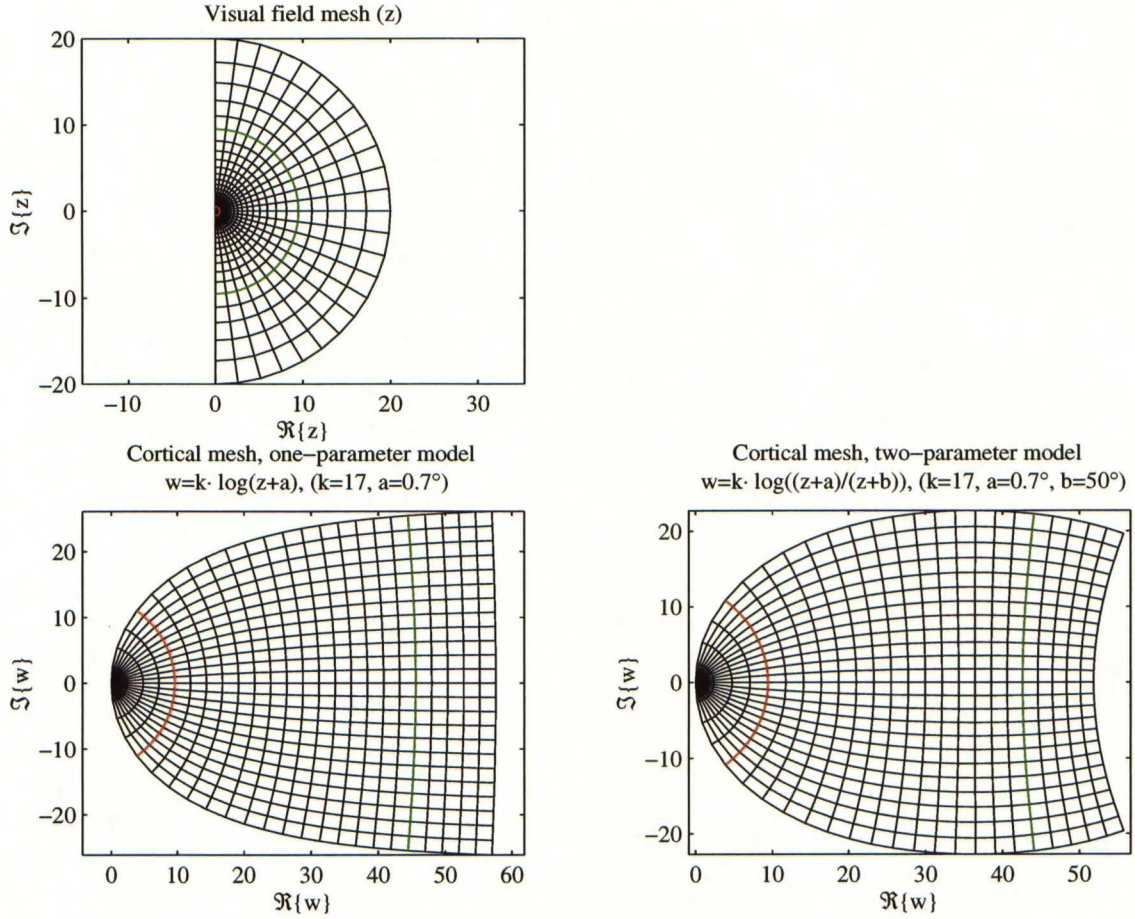


Figure 2.4: *The conformal mapping of points in the visual field (z) by one-parameter model $w = k \cdot \ln(z + a)$ and by two-parameter model $w = k \cdot \ln(\frac{z+a}{z+b})$ (\Re = real part, \Im = imaginary part). Two eccentricity lines are colored to emphasize the effect of cortical magnification near fovea.*

Conformal mapping approach was first applied to animal data [27]. These preliminary results demonstrated that conformal map of the visual field is a good approximation of the topographic map of the visual cortex. Recently conformal mapping method has been combined with human fMRI data [26].

Chapter 3

Principles of Magnetic Resonance Imaging

3.1 Nuclear Magnetic Resonance

Magnetic resonance imaging (MRI) is based on physical phenomenon nuclear magnetic resonance (NMR) [29]. Nuclei with odd number of nucleons (i.e. protons plus neutrons) have magnetic moment μ and spin, and thus interact with an external magnetic field \mathbf{B}_0 . MRI of human body mainly images NMR signal from hydrogen nuclei, because approximately 63 % of the atoms of human body are hydrogen atoms and hydrogen nucleus being a single proton has a magnetic dipole moment [30].

A proton tends to align with external magnetic field with net torque \mathbf{N} ,

$$\mathbf{N} = \mu \times \mathbf{B}_0. \quad (3.1)$$

Because of this torque, the proton precesses around the direction of the magnetic field at the so-called Larmor frequency

$$\omega_0 = \gamma B_0, \quad (3.2)$$

where γ is the gyromagnetic ratio. For hydrogen, the factor $\gamma/2\pi$ is 42.58 MHz/T. The Larmor frequency is the resonance frequency of the NMR, because nuclei can efficiently absorb and emit energy only at this frequency. [29, 31]

The thermal energy of a proton at human body temperature is huge compared to the energy associated with the parallel alignment of the magnetic dipole moment in an external field. Even then, an external magnetic field produces a slight magnetization M . In magnetic field of 1.5 T at room temperature, roughly 10^{-5} of hydrogen nuclei contribute to the magnetic resonance (MR) signal at each excitation [31].

3.2 Origin of MR Signal

At equilibrium, the magnetization aligns with the direction of magnetic field and there is no net transverse magnetization. The orientation of the precessing hydrogen nuclei can be changed by applying an RF pulse. The RF pulse is a magnetic field \mathbf{B}_1 perpendicular to \mathbf{B}_0 , oscillating at the Larmor frequency ω_0 . The amount of tilt of the magnetization (i.e. the flip angle) can be changed with the duration and amplitude of the RF pulse. [29]

The precessing transverse magnetization produces a changing magnetic field which is detected as NMR signal in a detector coil. The amplitude of the NMR signal is proportional to the strength of the transverse magnetization [29]. Once the RF pulse is removed, the transverse component of the magnetization decays exponentially. The detected NMR signal is called free induction decay (FID) signal.

The magnetization returns to equilibrium with the relaxation of the longitudinal component to its original value and the transverse component to zero. The longitudinal relaxation is also called spin-lattice decay because it arises from the interactions between spins and the atomic neighborhood; the excess energy absorbed from the RF pulse is emitted to the surroundings [29]. The associated time constant is called T_1 .

In a real sample, the applied magnetic field is not the only source of magnetic field, because at least the precessing nuclei themselves produce magnetic fields. These local magnetic field inhomogeneities cause the nuclei to precess at slightly different rates and individual nuclei start to disperse ('dephase') in time. Therefore, the transverse relaxation is also called spin-spin decay and the associated time constant spin-spin relaxation time T_2 . In human body, the applied magnetic field is not homogeneous and causes additional dephasing of the nuclei. Thus the transverse relaxation happens more quickly, with a time constant of T_2^* . T_2^* is a combination of T_2 and effects of local field inhomogeneities. For MR image contrast, it is essential that the relaxation times T_1 , T_2 and T_2^* are different between different tissues. [29, 31]

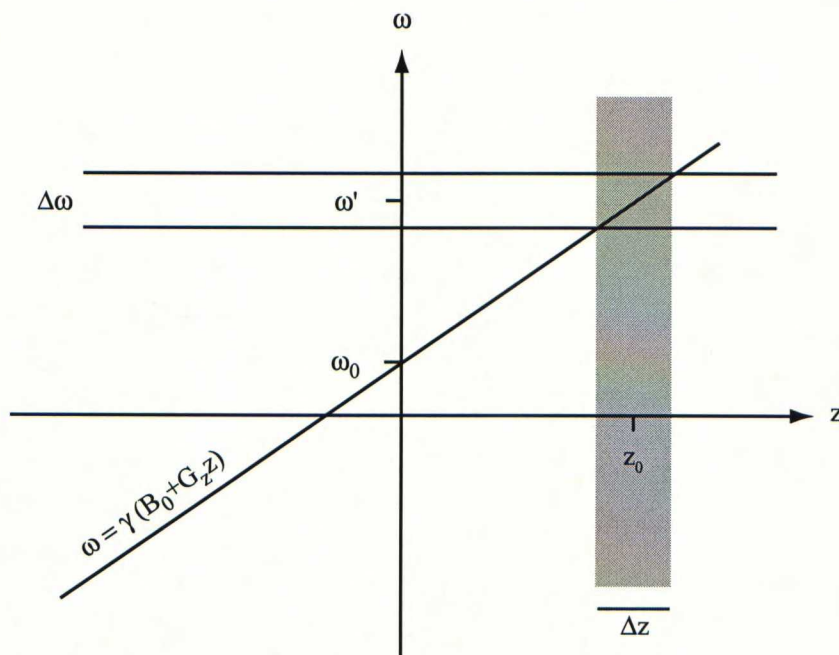


Figure 3.1: In slice selection a field gradient G_z is turned on along the z -direction. The location z_0 and width Δz of the slice are selected with the center frequency ω' and frequency band $\Delta\omega$ of the RF pulse [29].

3.3 Imaging Principles

The spatial encoding of the MR signal usually comprises of slice selection, frequency encoding and phase encoding. The direction of the slice selection is arbitrary in space; the corresponding axis is here labeled as z . The frequency and phase encoding directions are orthogonal to the slice selection direction and to each other, and are typically labeled as x and y directions. [29]

In slice selection, a magnetic field gradient G_z is applied along the z -axis. As result, the resonant frequency varies along this direction. A single slice can be excited with an RF pulse tuned to contain only a narrow range of frequencies with a center frequency at $\omega' = \gamma(B_0 + G_z z_0)$ [29]. The location of the slice at z_0 can be changed by changing the center frequency of the RF pulse (see Fig. 3.1).

After the RF pulse, a frequency encoding gradient G_x is turned on along the x -axis. In consequence, the magnetization vectors at different x -positions have slightly different resonant frequencies and precess at different rates (see Fig. 3.2) [31]. To unwind the phase offsets, an opposite polarity gradient in the same direction is turned on after the first frequency encoding gradient. The data acquisition is

commonly centered at the gradient echo occurring halfway through this second gradient pulse [31].

The remaining direction is localized with an additional field gradient G_y in the phase encoded direction (y -axis). This gradient is turned on after the RF pulse but before the data acquisition and modifies the phase of the signal [29]. The y -dependent phase difference remains locked in after the gradient G_y is turned off and the magnetization vectors again precess at the same rate. The amplitude of the phase encoded gradient is increased, stepped, every time the sequence is repeated. Hence, the phase differences between the signals at two positions increase linearly with time and each local magnetization is marked with a phase offset proportional to its y -position. Depending on the scan area and voxel size the phase encoded step is typically repeated 128 to 256 times to collect all the data needed [31].

In summary, with the slice selection, frequency encoding and phase encoding gradients the resonant frequency and phase of the magnetization vectors in different locations are changed. With Fourier analysis, the resulting NMR signal consisting of a mixture of signals at different temporal frequencies and phases can be split into independent signals from different locations.

The magnetic resonance data are collected in the so-called k -space. The general expression for spatial frequency vector $\mathbf{k}(t)$ is

$$\mathbf{k}(t) = \frac{\gamma}{2\pi} \int_0^t \mathbf{G}(t) dt, \quad (3.3)$$

where $\mathbf{G}(t)$ is the total field gradient vector and t is the gradient on-time. Increasing the product of gradient amplitude and time, the image resolution is increased. $\mathbf{G}(t)$ and the trajectory through the k -space are defined by the selected imaging sequence. [31, 32]

The signal from a single RF excitation is

$$s(\mathbf{k}) = \int \rho(\mathbf{r}) \exp(-i2\pi\mathbf{k} \cdot \mathbf{r}) d^3r, \quad (3.4)$$

where $\rho(\mathbf{r})$ is the spin density [29]. The reconstructed image $\hat{\rho}(\mathbf{r})$ is the inverse Fourier transform of the measured data $s_m(\mathbf{k})$ [29]

$$\hat{\rho}(\mathbf{r}) = \int s_m(\mathbf{k}) \exp(i2\pi\mathbf{k} \cdot \mathbf{r}) d^3k. \quad (3.5)$$

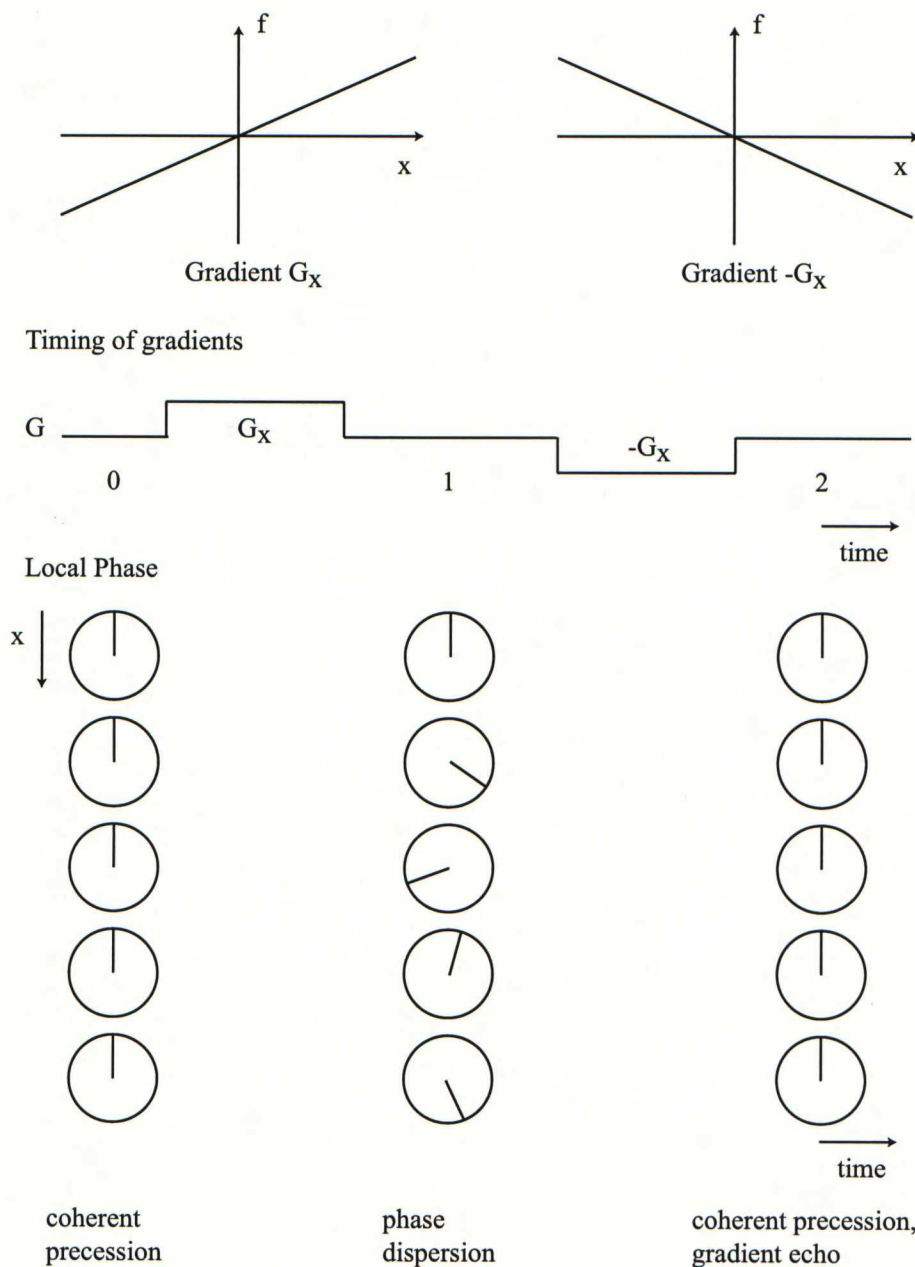


Figure 3.2: *Frequency encoding. Magnetization vectors precess at the same rate in a uniform field (time point 0). When a gradient is turned on the magnetization vectors at different locations precess at different rates. After the gradient is turned off, the magnetization vectors precess at the same rate but the phase angles are linearly proportional to the locations (time point 1). An opposite polarity gradient unwinds the phase offsets (time point 2) and a gradient echo occurs. Modified from Burton 2002 [31].*

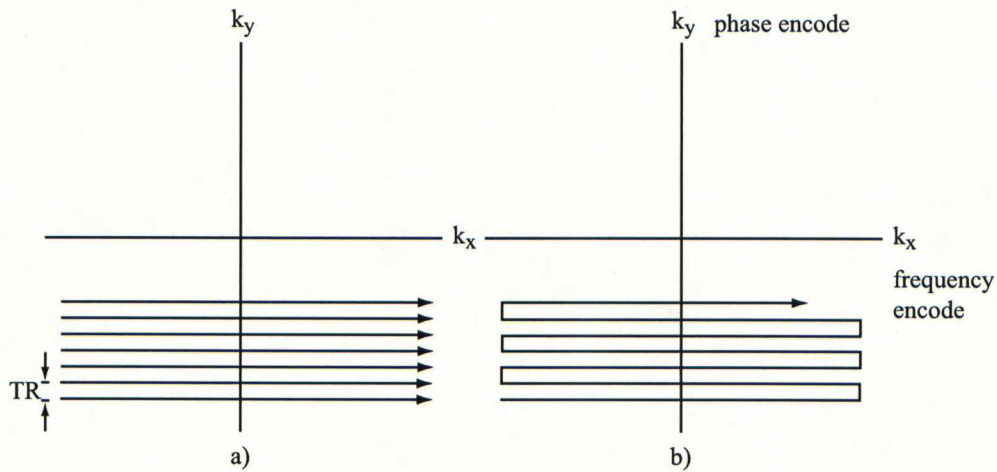


Figure 3.3: In a) conventional imaging each data line in the k -space is acquired with a separate RF pulse. In b) echo-planar imaging all the data lines follow a single RF pulse. EPI needs rapid switching of the frequency (readout) and phase encoding gradients. [32].

In conventional MRI, a separate RF excitation is required prior to collection of each data line. The total imaging time depends on the time between excitations (TR) and the total number of data lines defining the resolution. Echo-planar imaging (EPI) is a fast imaging sequence, where all data lines follow a single RF pulse (see Fig. 3.3) [32]. It requires high field gradients and rapid switching of the gradients.

3.4 MR Image Contrast

The main aim in MR imaging of human is to distinguish different tissues from each other, e.g. white matter from gray matter. This is possible because MR signal depends on various tissue parameters. In MRI, the imaging can be sensitized to different tissue parameters. Three common weightings measure spin density, T_1 and T_2 . The T_1 values for normal soft tissues are quite different from one another (see Table 3.1). Hence, different tissues can be efficiently delineated with T_1 -weighted contrast. The differences in T_2 values between tissues are smaller, but an elevated T_2 characterizes a pathological tissue and this is why T_2 contrast is found to be a sensitive indicator of diseased tissue. T_2^* contrast is sensitive to local differences of magnetic susceptibility between tissues, and therefore commonly used in fMRI studies. [29, 31]

The measured MR signal is always a function of many parameters (e.g. spin

Table 3.1: *The estimated T_1 , T_2 and spin density ρ_0 (relative to CSF) values at 1.5 T for white matter (WM), gray matter (GM), fatty tissue (FT) and cerebrospinal fluid (CSF) [29].*

Tissue	T_1 (ms)	T_2 (ms)	ρ_0
WM	600	80	0.65
GM	950	100	0.8
FT	250	60	0.9
CSF	4500	2200	1.0

density, T_1 , T_2 , T_2^*) [29]. To enhance differences between tissues with some contrast the imaging parameters must be optimized. In Table 3.2, some basic rules are presented, how imaging parameters, repetition time (TR) and echo time (TE), could be chosen to achieve different contrasts.

3.5 Basic Imaging Sequences

Two common MRI pulse sequences are the spin echo sequence and the gradient echo sequence. EPI can be used with either sequence. In typical spin echo (SE) imaging, after time $TE/2$ from the 90° RF pulse and the first slice selection gradient a 180° refocusing RF pulse and a second slice selection gradient are applied [31]. This second RF pulse creates an echo of the original FID signal (a spin echo) at a time TE after the original excitation pulse. SE sequence corrects the field

Table 3.2: *Principles of selecting imaging parameter repetition time (TR) and echo time (TE) when optimizing different contrasts [29].*

Contrast	TR	TE
T_1 -weighted	near to T_1 value	as short as possible
T_2 -weighted	as short as possible	near to T_2 value
Spin density -weighted	as long as possible	as short as possible

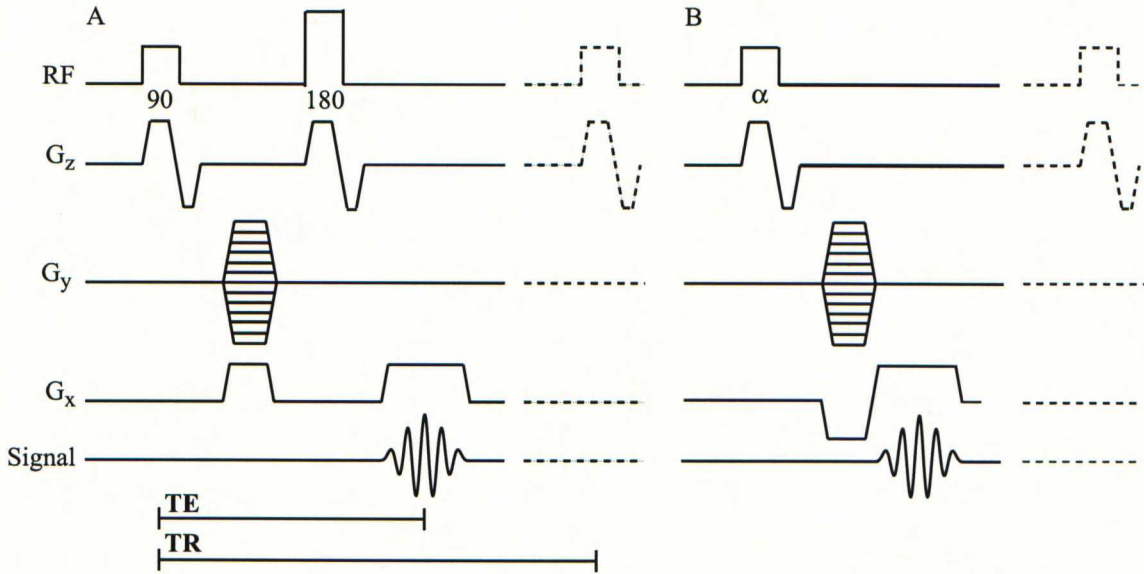


Figure 3.4: Timing diagrams of a) spin echo imaging sequence and b) gradient echo imaging sequence. The timings of radiofrequency pulse (RF), slice selection gradient G_z , phase encoding gradient G_y and frequency encoding gradient G_x are shown. The stepped timing pattern indicates that the amplitude of the G_y gradient is increased every step the sequence is repeated.

inhomogeneities and the SE signal decays exponentially with time constant T_2 [31]. The timing diagram for this spin echo sequence is shown in Fig. 3.4a.

RF energy, heating the subject's body, increases with the square of the flip angle [29]. In gradient echo (GRE) sequence, the flip angle of the excitation RF pulse can be reduced and there is no refocusing 180° RF pulse. So the TR can be made much shorter than with the SE sequence, because subject is deposited to much lower RF energy dose than with SE sequence [31]. The timing diagram for gradient echo sequence is shown in Fig. 3.4b.

When TR is very short, each RF pulse both creates an FID and generates echoes of the previous FIDs [31]. So the net signal after each RF is a sum of FID from the most recent RF plus echoes from previous FIDs. The signal decays with a time constant T_2^* [31].

With short TR, there exist three main types of GRE sequences [31]. The net GRE signal is measured with a steady state sequence, usually called gradient-recalled acquisition in the steady-state (GRASS) or fast imaging with steady-state precession (FISP). In spoiled sequences (SPGR or FLASH), a spoiler gradient is applied to cancel the echo component of the signal. With a steady-state free

precession (SSFP) sequence, a spoil gradient destroys the FID from the most recent RF pulse and only the echoes contribute to the measured signal.

When the flip angle is small the echo component of the signal is weak. Then there is not much difference between steady state GRE signal and spoiled GRE signal and both are primarily spin density -weighted [31]. With larger flip angle the echo component becomes larger than the FID signal from the most recent RF pulse. Steady-state GRE signal is now much larger than spoiled GRE signal, but because steady-state signal contains both T_1 and T_2 weighting, tissue contrast can be better with T_1 -weighted spoiled signal [31].

Chapter 4

Functional Magnetic Resonance Imaging

4.1 Physiological Changes in Brain During Neural Activation

In particular excitatory and inhibitory synaptic activity, rather than action potentials, increase the energy consumption of brain. This increased energy demand is mostly met by oxidative glucose consumption. At the onset of neural activity, a signal is sent to the smooth muscles of arterioles feeding the active population of neurons. The local arterioles dilate which leads to an increase in local blood flow. The increase in blood flow is larger than the increase in oxygen consumption, causing increase of the local oxygenation in the active brain area. [33]

The neuronal events occur on a time scale of milliseconds, but the metabolic and vascular events happen on a time scale of seconds. Hence, precise temporal information is lost with fMRI. However, even a very brief neuronal event, on a scale of milliseconds, induces metabolic needs and corresponding vascular changes. The spatial resolution of fMRI is very good compared to other noninvasive functional imaging modalities. The spatial extent of the activated area can be well delineated and the activation can be precisely matched to the anatomical structures. Nevertheless, some loss of spatial resolution is associated with the blurring of the neural activity to a vascular event. [33]

4.2 Blood Oxygenation Level Dependent Signal

Hemoglobin is the main oxygen carrier in blood. In oxygenated state hemoglobin is diamagnetic, and hence fully oxygenated blood has about the same susceptibility as other brain tissues. Deoxygenated hemoglobin is paramagnetic, and because of the difference in the magnetic susceptibility relative to surrounding brain tissue a magnetic field distortion is induced. The basis of blood oxygenation level dependent (BOLD) contrast in fMRI is this susceptibility difference induced field distortion. Due to distortion, the local MR signal is decreased, i.e. when neurons activate causing excess local blood flow local signal increases due to increase in the amount of oxygenated hemoglobin. [34]

Most current fMRI studies, based on BOLD contrast, are usually measured with the GRE sequence, because it is much more sensitive to the BOLD effect than the SE sequence. Relaxation time T_2^* contrast is sensitive to local magnetic field susceptibility differences; T_2^* shortens in the presence of deoxygenated hemoglobin and lengthens when oxygenation increases. Therefore, the T_2^* -weighted GRE-signal increases with a longer T_2^* . [31]

4.3 Experimental Design

In block design of a functional MRI experiment, relatively long periods of task performance alternate with control periods. Each block of task performance consists of several trials of the same kind, presented together. These blocks are designed to evoke a particular cognitive or sensory process. The control periods between task performance are designed to evoke all the other neural processes present except the process of interest. The sensitivity of the block-design experiment is maximized when the evoked hemodynamic responses are as homogeneous as possible. The statistical power of block design is superior to other fMRI designs [35]. This is because the frequency of the stimulation in block design can be concentrated in the low noise range. However, the evoked responses can decrease in time because the trial events are predictable and thus the neural systems habituate. When there are more than two conditions in the block design, the blocks could be randomized, but then the variance is distributed and statistical power decreases. The disadvantage of block design is that the trials of the same type are always grouped in time excluding studies of single epochs. [36]

The transient neuronal changes associated with single cognitive or sensory events can be studied with event-related fMRI. This allows more flexibility in the exper-

imental design because the trial presentations can be randomized. A brief period of neural activity eliciting detectable hemodynamic response can be evoked with a very rapid stimulation ($\ll 1$ s) [37].

In event-related fMRI experiments, the design and data analysis are usually based on the knowledge of the characteristics of the BOLD response. Based on the timing of the stimulation, the responses are selectively averaged and/or explicitly modeled for each different type of events (see Fig. 4.1). Several analyses are based on the correlation of the observed event-related response to a model of the expected hemodynamic change. The main characteristics of the hemodynamic response, the shape and time course, can be well modeled. A hemodynamic response can be modeled with an impulse function (see Fig. 4.1a). After the onset of the stimulation there is a delay in the onset of BOLD response and a poststimulus undershoot after the primary positive change. In addition, several groups have reported a dip in the BOLD signal before the positive change. [37]

There is variability across subjects in the shapes of the evoked hemodynamic responses [38]. The evoked hemodynamic response within a single subject can also vary from one day to another, but to a lesser extent [38]. Variation in the hemodynamic response has also been observed across brain regions [39]. It is still unclear whether variation in the hemodynamic response reflects differences in the underlying neurovascular coupling or real delayed neuronal activity [37].

Neural responses coupled with stimulation and the corresponding BOLD responses are considered linearly additive. That is, the neural response will roughly summate on top of the previous response. With high stimulus presentation rates this linearity approximation is not valid, but with typical presentation rates (one event per 2 seconds or less in time) the linearity can be assumed [37].

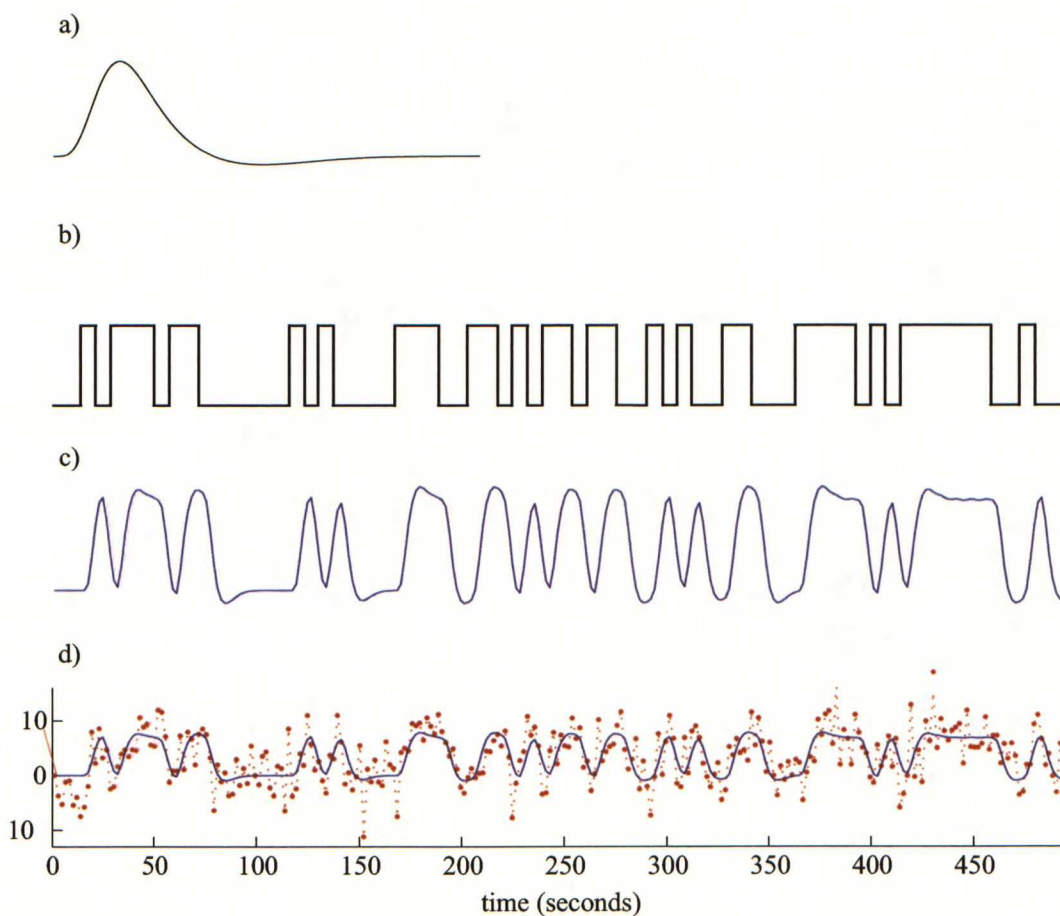


Figure 4.1: a) The characteristics of a hemodynamic response can be modeled with an impulse function consisting of two gamma functions. b) An example stimulation pattern is c) convolved with the hemodynamic response function. d) Raw data from one voxel and the fitted response.

Chapter 5

Phase Encoding Retinotopic Approach and Multifocal fMRI

5.1 Phase-Encoded Retinotopic Mapping

Because of the retinotopic organization of the human visual cortex, a periodic stimulus in the visual field moving from foveal to more peripheral region generates a wave of neural activity along the calcarine sulcus [18]. This kind of neural activity is detected in fMRI as wavelike progressing BOLD signal [3]. The phase of this BOLD signal encodes position in visual field. Both the response amplitude and phase can be calculated with discrete Fourier transform

$$F_{\nu_0}(\mathbf{x}_j) = \sum_{k=1}^N f(\mathbf{x}_j, t_k) \exp(\pm i 2\pi \nu_0 (t_k - t_H)), \quad (5.1)$$

where ν_0 is the stimulus frequency, \mathbf{x}_j the voxel positions, N is the number of volumes, t_k are the instances of acquisition of the functional volumes, t_H is an estimation of the mean hemodynamic delay and f is the raw functional data [3, 20].

In phase-encoded retinotopic mapping, the eccentricity of the visual field is mapped with concentric expanding and contracting rings and the polar angle of the visual field with clockwise and counterclockwise rotating wedge-shaped checkerboard stimuli (see Fig. 5.1) [24, 20]. The visual field representation changes from mirror symmetric to nonmirror symmetric from one retinotopic area to the neighboring visual area [24]. Hence, borders between the visual areas can be mapped accurately based on the information that this visual field sign (mirror symmetry vs.

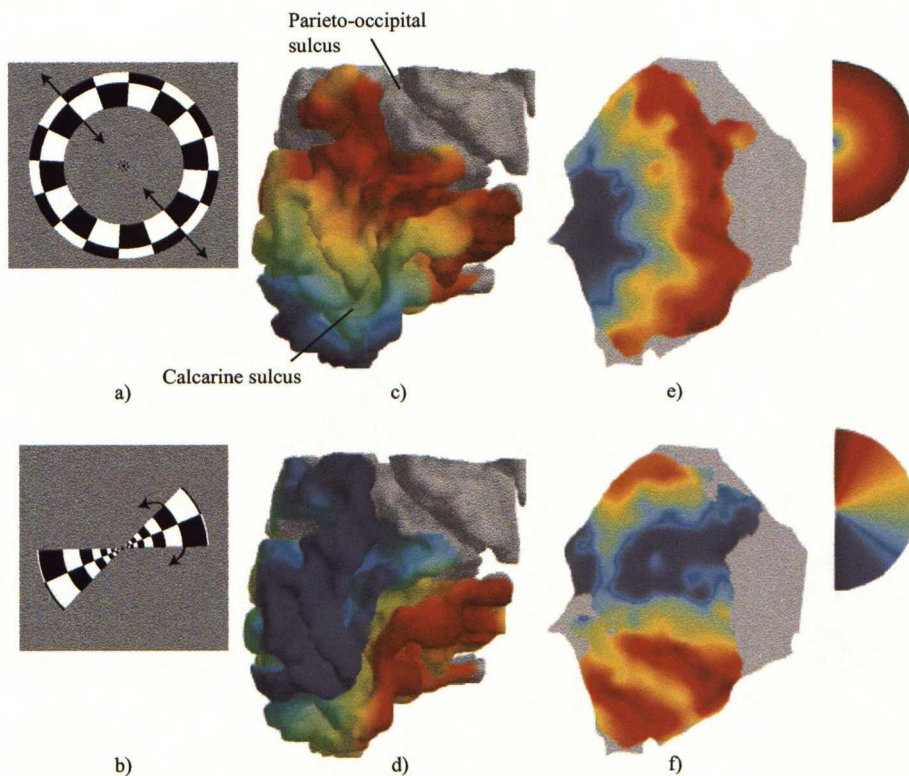


Figure 5.1: *In phase-encoded retinotopic mapping the visual field representation in the cortex is mapped with a) concentric expanding and contracting rings and b) clockwise and counterclockwise rotating wedge-shaped checkerboard stimuli. The response phases coding c) the eccentricity and d) the polar angle of the visual field are assigned to subject's reconstructed occipital white-matter gray-matter -border. e) The eccentricity map and f) the polar angle map is shown on subject's unfolded cortical surface.*

nonmirror symmetry) changes in the border [24].

The phase-encoded retinotopic method relies in most cases on the segmentation and reconstruction of the anatomical MRI data [3]. That is, the phase-encoded data are typically represented on the reconstructed and unfolded cortical surface of the subject. Recently, a volumetric segmentation approach for mapping human visual retinotopic cortex has also been introduced [40]. Even so, with phase-encoded approach only the borders between low-order visual areas can be mapped accurately, but the location of visual field representation within a visual area is confounded with both local (signal-to-noise -related) and global (offset) phase uncertainties.

5.2 Background of Multifocal Method

Multifocal approach refers to the concurrent characterization of response properties of multiple retinal or visual field locations [1]. Sutter [41] and others have successfully used the multifocal m-sequence (maximal length sequence) technique in many studies of electroretinograms.

In the multifocal electroretinogram (mfERG), a large number of retinal locations are stimulated pseudo-randomly, based on the m-sequence. Retinal locations are typically stimulated with a pattern of hexagon shaped elements (see Fig. 5.2a). The illumination of a hexagon follows the m-sequence and in each frame a hexagon has a 50 % chance of being illuminated. The retinal cells respond to the changing lighting conditions and this can be measured with an electrode. The focal responses of these retinal locations are calculated by correlating the continuous ERG signal with the stimulation sequence. With mfERG, a topographic map of ERG responses can be constructed.

Multifocal m-sequence technique has also been introduced for visually evoked potential (VEP) studies. In mfERG the stimulated locations are usually equally sized, but in multifocal VEP (mfVEP) the stimulated visual field regions are scaled based on the cortical magnification in the human visual cortex (see Fig. 5.2b) [42]. This is done to activate equal sized patches in the visual cortex. During the stimulation in mfVEP the checkerboard pattern reverses in contrast according to m-sequence [42]. The multifocal m-sequence technique is implemented in the commercially available VERIS (Electro-Diagnostic Imaging Inc., San Mateo, CA) system.

James [2] has developed pattern-pulse multifocal VEP in Matlab environment. The visual field regions are stimulated with pulses of pattern contrast (see Fig. 5.2c). When compared to the results with contrast-reversing multifocal approach, the pattern-pulse responses have 15 times larger amplitude [2]. In practice, this means that the stimulation time with pattern-pulse multifocal VEP can be much shorter than with contrast reversing mfVEP for acquisition of equal signal-to-noise-ratio responses.

Both mfERGs and mfVEPs are intensively used in basic research and in clinical applications. The field topography of mfERG responses has been studied and there has been an attempt to map the retinotopic organization of visual cortex with mfVEP [43, 44]. With multifocal techniques, retinal and optic nerve dysfunctions can be efficiently diagnosed [45, 46].

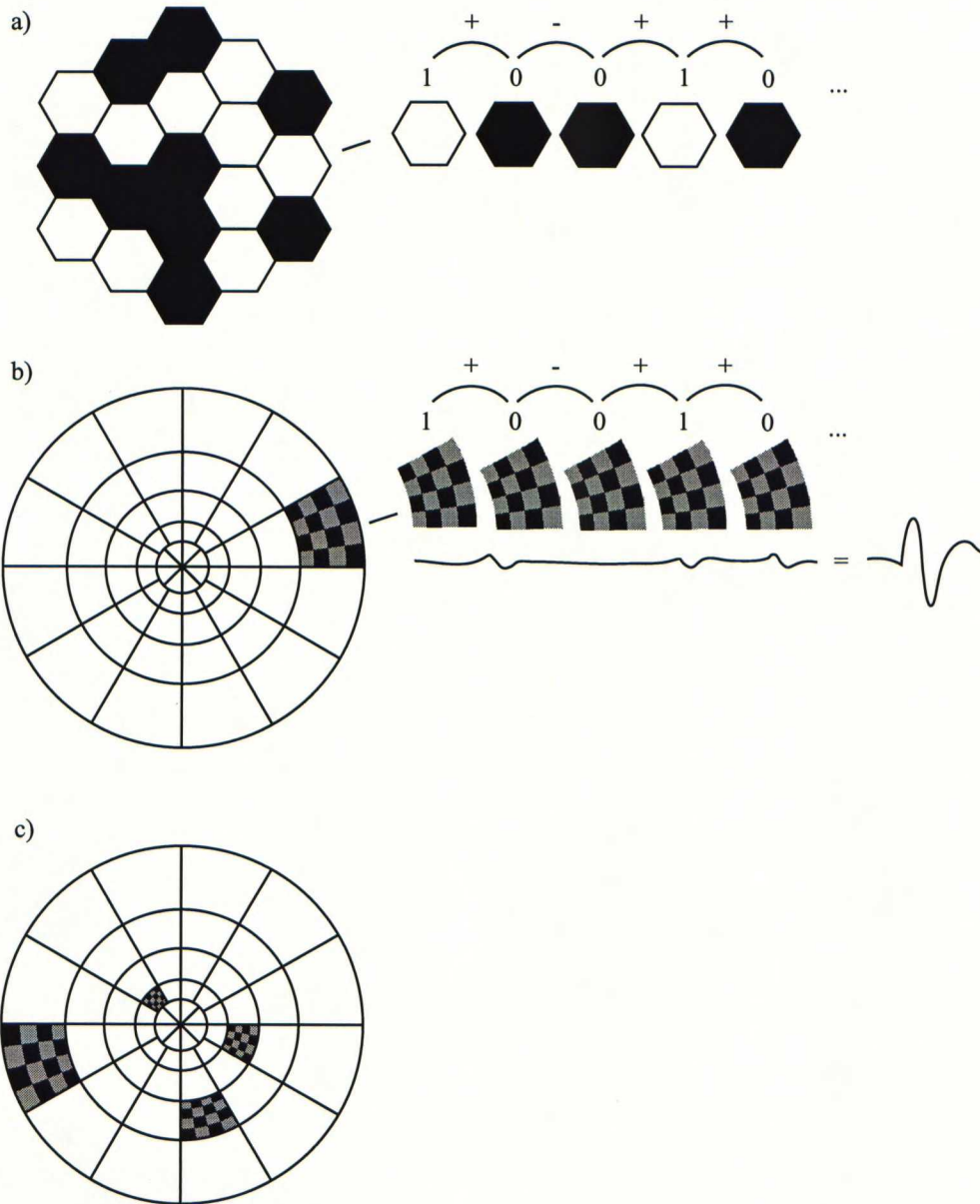


Figure 5.2: a) In *mfERG*, the illumination of the hexagon shaped elements follows the *m*-sequence [1]. b) In *mfVEP*, the checkerboard pattern reverses contrast determined by the *m*-sequence [42]. As an example only one region is shown. c) In pattern-pulse multifocal VEP with each frame one or more visual field regions are stimulated with brief pulses of pattern contrast with mean luminance background in-between [2].

5.3 Multifocal fMRI

Our aim has been to introduce multifocal approach for fMRI. The idea is the same as with multifocal VEP, but the spatial resolution of fMRI is superior to electroencephalography (EEG). So, multifocal fMRI can reveal detailed information of the retinotopic representation of the visual field in single individuals.

In conventional block design of fMRI, where multiple visual field locations would be stimulated in turn, it is not possible to stimulate as many visual field regions as with mffMRI, at least not in a reasonable measurement time. In addition, the analysis of multifocal data is straightforward, so there is no need for Fourier analysis as with the phase-encoded approach. Instead, statistical approaches based on standard model can be used. In practice, this enables retinotopic mapping with all standard fMRI software without need for specific skills. Because the multifocal responses are discrete, there is no possibility of error in the phase assignment. Therefore, from multifocal responses it is straightforward to detect distortions in retinotopic representation and possible missing local responses.

The statistical 3D analysis of multifocal fMRI can be automated which is important for the potential clinical use. Only the coregistration of the functional and anatomical images has to be checked. After statistical analysis, the locations, strengths and extents of the responses can be studied. In contrast with phase-encoded mapping, all retinotopic areas and low signal-to-noise voxels contribute to activation map, impairing discrimination of functional areas in 3D-view.

Only retinotopic visual areas can be mapped with mffMRI, because multifocal signals from nonretinotopic areas are correlated and can not be identified from the multifocal data. In addition, to characterize retinotopic organization in a visual area, stimulated regions should be large enough to evoke a detectable signal. The receptive field size is smallest in V1 and increases towards higher order visual areas; thus largest number of neurons and the strongest signals are expected from V1 with mffMRI.

Because the human visual cortex is highly folded and the visual areas lie deep in the calcarine sulcus, it is worthwhile to segment and reconstruct subject's visual cortex to study more closely the locations of activations. On the unfolded cortical surface, the representations of a local visual field region in several visual areas can be visualized simultaneously. As well, the local responses from stimulations of multiple visual field regions can be visualized simultaneously to study the retinotopic organization within a visual area.

The function of human visual cortex is difficult to study with magnetoencephalog-

raphy (MEG) and EEG, because functionally different visual areas are tightly located in the back of the head and active in parallel [47]. A priori information on the active loci in cortex would help in the analysis. From fMRI results combined with reconstructed cortex, a priori information about the position and orientation of the source can be derived [47, 48]. With mffMRI it should be possible to find visual field areas whose dipoles representing activations in visual areas V1, V2 and V3 are spatially orthogonal. MEG/EEG signal separability can be improved with these orthogonal dipoles in visual areas.

Chapter 6

Materials and Methods

6.1 Stimulus and Subjects

In our stimuli the visual field between 1-12 degree radius is divided into 60 regions (see Fig. 6.1). In principle, there are no a priori limitations due to multifocal method for the width of the visual field or to the number of stimulated regions. In our case, the visual field is limited by the dimensions of the magnet bore.

Andrew James (Australian National University, Canberra, Australia) made the multifocal stimuli to our study. The following description of the stimuli is based on personal communication with A. James. The stimulated regions are scaled according to human magnification factor to activate equal sized patches in the cortical surface [26]. The stimulation sequence is based on quadratic residue sequence

$$t = j^2 \bmod N \tag{6.1}$$

where the length of the sequence N is a prime of form $4K - 1$ (K integer) and j is a set of integers from 0 to $N-1$.

The length of our stimulus sequence is 67. This prime gives a suitable length to our experiment. When constructing the stimulation sequence for one region the values of sequence $X_1(t)$ are set to -1 from 0 to 66. Then the values are set to 1 for $t = j^2 \bmod 67$ where j is from 0 to 66. Region 1 in the multifocal stimulus is active when $X_1 = 1$.

When constructing the stimulation sequence for the second region in the multifocal stimulus the stimulation sequence is delayed by a shift. To assure that the signals

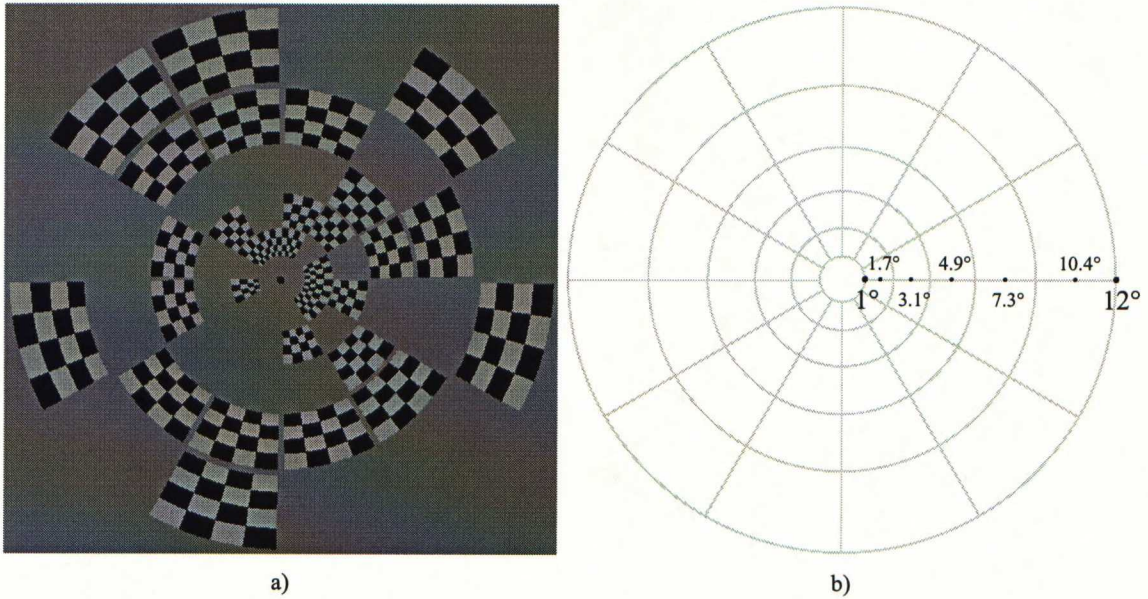


Figure 6.1: a) An example frame of our multifocal stimulus. b) At a viewing distance of 35 cm the stimulated visual field covers 1° – 12° from the fovea.

from two neighboring regions are well removed the shift of 17 steps was chosen. In addition, with 17 being a prime, no two regions of the 60 regions in the stimulus will have the same shift. So, the stimulation sequence for the second regions is $X_2 = X_1(t - 17 \bmod 67)$ and the sequences for the rest of the regions are cyclically delayed by another 17 steps.

In Fig. 6.1a, an example frame of our multifocal stimulus is presented. Overall, the stimulus consists of 67 bitmap images like the one shown in the figure. With each image half of the visual field regions are stimulated, so each region is stimulated approximately half of the stimulation time. During the stimulation the checkerboard pattern reverses contrast at 8 Hz.

Six subjects (3f, 23-39 years) with normal or corrected to normal vision participated the study. The stimulus was presented with Presentation™ software (Neurobehavioral Systems, Inc.) and delivered with a data projector (Christie Vista X3, Christie Digital Systems, Inc.). Subject viewed the stimulus via a mirror with a viewing distance of 35 cm and were asked to fixate on a black spot in the middle of the stimulus.

Table 6.1: *The main imaging parameters used in the high resolution (HR) and low resolution (LR) structural data acquisitions (TE echo time). The number of slices N , slice thickness d and field of view FOV define the scan volume. The voxel size is determined with the FOV, matrix and slice thickness.*

	N	TE (ms)	FOV (cm)	d (mm)	Matrix	Voxel (mm ³)
HR	124	minimum	23	0.9	256×256	0.9×0.9×0.9
LR	124	minimum	23	1.5	128×128	1.5×1.8×1.8

6.2 Data Acquisition

The subjects were examined with a 3T whole-body MRI scanner (General Electric Inc., Signa VH/i) equipped with a head volume coil. In the functional data acquisition, we used single shot gradient-echo echo-planar imaging sequence. In the structural data acquisition, we used spoiled gradient echo sequence. All the subjects participated in two measurement sessions. In the first experiment, the retinopy was mapped with the phase encoding stimuli. A high resolution anatomical image was acquired in the same session to allow optimal segmentation of the white/gray matter border and later surface-oriented analysis with 3D and 2D cortical surface models. In the multifocal experiment, a low resolution anatomical image was acquired for coregistration of the functional scans with the high resolution structural image and corresponding segmented cortical surface models. The main imaging parameters for the structural data acquisitions are shown in Table 6.1.

In the multifocal setup, after localizer images, four series of functional data, magnetic field map using asymmetrical spin echo and the low resolution structural data were acquired. The imaging parameters for the functional series are shown in Table 6.2. During the functional data acquisition, the subjects viewed the multifocal stimulus.

Because of the magnetic saturation effects, the scans during the first four TRs are excluded from the statistical analysis, and the stimulation begins after these scans. Every image in the multifocal stimulus is on for four TRs (4 times 1.819 s). In the end of the functional series for four TRs the subject views a display with only fixation on without any stimulation. Hence, each functional time series comprises of 276 volume images and the imaging time for the functional series was four times 8 min 22 s.

Table 6.2: *The imaging parameters for the functional (F) data acquisition. TR is the repetition time and α the flip angle.*

	N	TR (s)	TE (ms)	α	FOV (cm)	d (mm)	Matrix	Voxel (mm ³)
F	124	1.819	40	90	16	2.5	64×64	2.5×2.5×2.5

6.3 Preprocessing of Data

The genesis format functional data and dicom format structural data were converted to analyze format with SPM2 (Wellcome Department of Imaging Neuroscience, London, England, [49]) Matlab toolbox. Head motion creates artifact to the analysis of functional series. Therefore, motion correction was applied for the functional data using SPM2 software. An interleaved echo-planar imaging sequence was used in functional data acquisition. Slice time correction using SPM2 was applied to correct the differences in the image acquisition times. As reference slice, the middle slice in time was used. For each subject a magnetic field map with asymmetrical spin echo sequence was also acquired during the measurement session [50]. With this field map, the field distortions induced by susceptibility inhomogeneities were corrected [50].

6.4 Statistical Analysis of Functional Data

Data were analyzed by means of statistical parametric mapping using SPM2. In statistical parametric mapping, hypothesis about regionally specific effects in the functional data are tested. Each voxel is analyzed separately using a statistical parametric test (e.g. t-statistic) and the resulting statistics are fused into an image. The image is interpreted as a spatially extended statistical process and called statistical parametric map. [51]

Most statistical parametric maps are based on linear models, t-statistic, and correlation coefficient analysis, which are all special cases of the general linear model (GLM) [51]. The gaussian random field theory (GRF) is used in the multiple comparison problem of simultaneously assessing all the voxel statistics [51]. SPM2 software implements both GLM and GRF [49].

In GLM, the measured data are modeled as a linear combination of model functions

and random noise. GLM is expressed as

$$\mathbf{Y} = \mathbf{X}\beta + \epsilon, \quad (6.2)$$

where matrix \mathbf{Y} contains the observed responses, design matrix \mathbf{X} contains the explanatory variables, β is the parameter vector containing the unknown weights β_i to be estimated for each voxel and ϵ is the error matrix [51]. The first assumption is that the error terms are identically and independently distributed (i.e. i.i.d, $\epsilon(t) = N(0, \sigma^2 I)$).

The least-squares estimate of β is

$$\hat{\beta} = (\mathbf{X}^T \mathbf{X})^{-1} \mathbf{X}^T \mathbf{Y}. \quad (6.3)$$

Then, the predicted response is

$$\hat{\mathbf{Y}} = \mathbf{X}\hat{\beta} = \mathbf{X}(\mathbf{X}^T \mathbf{X})^{-1} \mathbf{X}^T \mathbf{Y}. \quad (6.4)$$

and the estimated residuals are

$$\hat{\epsilon} = \mathbf{Y} - \hat{\mathbf{Y}}. \quad (6.5)$$

The parameter vector $\hat{\beta}$ is estimated by minimizing

$$\sum_{t=1}^N \hat{\epsilon}_t^2, \quad (6.6)$$

where N is the number of time points.

Better statistical models are obtained when the temporal pattern of the stimulation \mathbf{X} is convolved with the hemodynamic response function (hrf, $h(t)$). The modeling of the hrf with two gamma functions has been found to be reasonable and comprehensive model of the hemodynamic response. To allow more flexibility for the hemodynamic response in the latency and spread in time, derivatives of hrf can be included. The hrf is build up of temporal basis functions b_i

$$h(\tau) = \beta_1 b_1(\tau) + \beta_2 b_2(\tau) + \dots \quad (6.7)$$

The observed response in a voxel is then

$$y(t) = h(\tau) \otimes x(t) + \epsilon, \quad (6.8)$$

where \mathbf{x} is the timing of the stimulus. [37]

There may be noise components which correlate with the hemodynamics. These can not be removed with high pass filtering because they are in the same frequency range as the effects of interest [52]. This kind of noise induces temporal correlation in the residual error term ϵ and the i.i.d assumption does not hold [52]. In SPM2 these serial correlations are estimated with a restricted maximum likelihood (ReML) algorithm. ReML is an iterative method which allows simultaneous estimation of model parameters and autocorrelation parameters [52]. An autoregressive AR(1) model is used in SPM2

$$\mathbf{Y} = \mathbf{X}\beta + \mathbf{z}_1 + \mathbf{z}_2, \quad (6.9)$$

and

$$\mathbf{z}_1 = \mathbf{A}\mathbf{z}_1 + \mathbf{w}, \quad (6.10)$$

where $\mathbf{w} = N(0, \sigma_1^2 I)$ and $\mathbf{z}_2 = N(0, \sigma_2^2 I)$ [53, 54].

In a simple model, the measured signals from a voxel are divided into two groups of observations (rest and active). The t statistics can be used to test whether there is a significant difference between the means of these groups. When analysing neuroimaging data the null hypothesis, $\beta_i = 0$ (no activation), is tested. Using the GLM this is done by comparing the estimated parameters $\hat{\beta}$ and using linear contrasts c . The t value for a voxel is defined

$$t = \frac{c^T \hat{\beta}}{\sqrt{\text{Var}(c^T \hat{\beta})}}. \quad (6.11)$$

The t values are calculated for all the voxels [51]. These values form a statistical parametric map (SPM{t}-map) [55].

When testing the null hypothesis, the statistic value in a voxel can be compared to the null distribution to estimate the probability that this statistic could have occurred by chance. A critical height (t value) threshold is applied separately to

all of the statistical values to localize the brain activation. In SPM2, the p-value associated to this threshold t value is called the 'uncorrected' p-value. Typically the SPM $\{t\}$ -map consists of many thousands of voxels and without a priori information the hypothesis refers to the whole SPM $\{t\}$ -map. The multiple comparison problem in functional neuroimaging is that we have to decide, if this huge volume shows any evidence of the effect of interest. The Family-Wise Error (FWE) rate handles the likelihood that a family of voxel values could have occurred by chance. The Family-Wise null hypothesis is that the activation is zero everywhere. A critical height (t value) is applied to all of the statistical values, so that the probability that any of these values could occur above the threshold by chance is small. This is the 'corrected' p-value in SPM2. [56]

Bonferroni correction is a simple FWE rate thresholding method

$$p_{FWE} \leq n\alpha, \quad (6.12)$$

where p_{FWE} is the FWE rate, n number of tests (i.e. number of statistical values) and α a probability threshold. When a particular FWE rate is wanted, then the threshold for a single voxel is

$$\alpha = \frac{p_{FWE}}{n}. \quad (6.13)$$

Bonferroni correction is used in some imaging studies, but it is really suitable only for independent tests. The neighboring voxels are not independent but are spatially correlated and the Bonferroni correction is in most cases too conservative method. The probability values (p-values) for the smooth search volume of brain images can be corrected with random field theory (RFT). The probability of a FWE given by RFT is approximately equal to the expected Euler characteristics

$$p_{FWE} \simeq E[EC] = \sum_{d=0}^D R_d EC_d \quad (6.14)$$

where D is the number of dimensions, R_d the number of d -dimensional resolution elements and EC_d the d -dimensional Euler characteristics density [57]. The number of resolution elements, resels, is an approximation of independent elements. The Euler characteristics density is a property of an image after the image has been thresholded. The simplified idea is that after thresholding, the image consists of blobs and holes and Euler characteristics density is the number of blobs as a function of the threshold. We can set a particular threshold (e.g. $p_{FWE}=0.05$)

and then conclude that any remaining blob have a probability of less or equal to this threshold to occur by chance. Actually, the expected Euler characteristic does not depend only on the number of resels in the search volume but on the volume, surface area and diameter of the search region [57]. These parameters as well as the smoothness can be estimated from the image. [56]

In addition to FWE correction, it is possible to use False Discovery Rate (FDR) for the multiple comparison problem in functional neuroimaging data analysis. As the FWE correction controls the likelihood of any false positives, FDR gives the proportion of false positives among the suprathreshold voxels [58]. So, the null hypothesis is rejected for these voxels even though it is actually true. FDR is less strict correction method than FWE [58]. In the interpretation of results with FDR correction, it must be remembered that false positives will be detected and only the probability of them is controlled.

6.5 Surface Oriented Analysis

We used in the surface oriented analysis Brain à la Carte (BALC) Matlab toolbox [3]. With BALC, the structural MRI can be segmented and the reconstructed cortex unfolded. This toolbox is designed for the Fourier analysis of phase-encoded retinotopic mapping. However, with BALC any functional data can be assigned into the reconstructed cortex.

When the analysis concentrates on retinotopic visual areas, it is reasonable to reconstruct only part of the occipital lobe. Then the entire unfolded volume can be visualized simultaneously and no connectivity is lost [3]. The reconstructed cortex corresponds to the center of the segmented gray matter and is represented in approximately 20000 nodes with distinct 3D and 2D positions and determined neighborhood [3].

Amplitude and distance thresholds are used in the projection of the functional data to the surface of the reconstructed cortex. With amplitude (signal-to-noise) threshold, significantly activated voxels in the 3D surface are identified from the functional data [3]. The closest node (in 3D space) of the reconstructed surface is determined for each of these voxels. The functional information is attributed to the node, if the distance between the node and activated voxel does not exceed a defined distance threshold. The functional data was unsmoothed, because smoothing might have displaced the data for example through a gyrus or across a sulcus. Along the surface, the data were smoothed with a Gaussian kernel of 1.5 mm. A t value threshold of 1.5 and a distance threshold of 2.5 mm are used

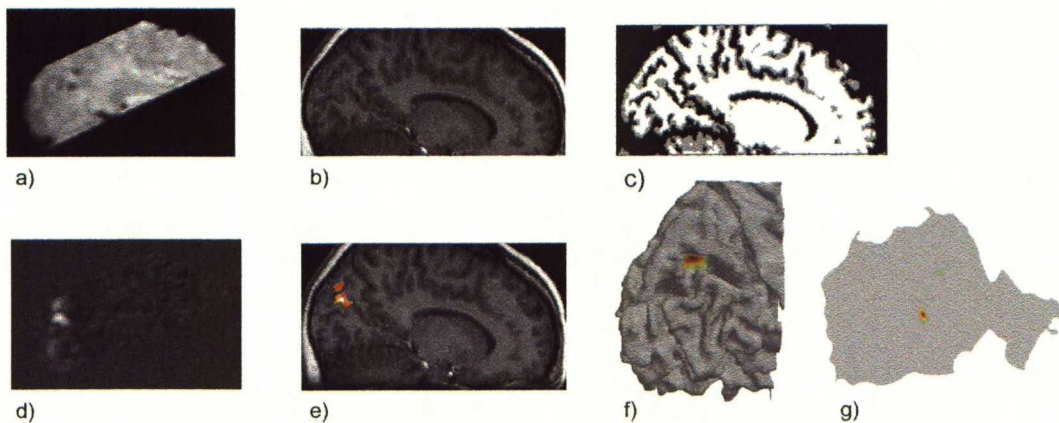


Figure 6.2: a) The BOLD sensitive fMRI data are analyzed by means of statistical parametric mapping to obtain statistical parametric maps (d) SPM{t}-map) b) The high resolution structural data is c) segmented. c) The segmented gray/white matter border of the occipital lobe is f) reconstructed and g) unfolded. d) The SPM{t}-map is e) thresholded and shown over the structural data and f) assigned to the reconstructed and g) unfolded cortex.

in the surface oriented analysis of multifocal data.

It is interesting to calculate the cortical surface area of V1. From the cortical surface areas devoted to various multifocal responses it is possible to study the inhomogeneities in the retinotopic representations. The surface area of a region of interest is approximately the sum of the areas of the triangles constituting the surface. This area A can be calculated using Heron's formula

$$A = \sum_{i=1}^n \sqrt{s_i(s_i - a_i)(s_i - b_i)(s_i - c_i)}, \quad (6.15)$$

a_i , b_i and c_i are the lengths of the sides of triangle i , n is the number of triangles and s_i is

$$s_i = \frac{a_i + b_i + c_i}{2}. \quad (6.16)$$

Chapter 7

Results

7.1 Statistical Results of Multifocal Data

For all the subjects all the 60 stimulated visual field regions produce clear, statistically significant ($p_{\text{FWE}} < 0.05$) response. The statistically most significant responses are in the occipital cortex, roughly located, as expected, according to the visual field position. Fig. 7.1 shows examples of activation patterns.

From 3D statistical results it is difficult to see where the activations precisely are. The locations of the clusters in Fig. 7.1 compared to the anatomical landmarks, such as calcarine sulcus, suggest that responses are coming from low-order visual areas. But to take a closer look to the response locations, we proceeded to the surface oriented analysis.

7.2 Surface Oriented Results

The statistical results (SPM{t}-maps from statistical analysis on SPM2) were assigned into the segmented and reconstructed occipital cortices of each individual subject. Surface oriented analysis was first done to the phase-encoded retinotopic mapping data and then to the multifocal data. An example of activation pattern for the subject MU in the reconstructed cortex, in 2D and 3D, is shown in Fig. 7.2. As expected, when the stimulated region was in the upper right hemifield, the activated clusters are in the left occipital cortex below the calcarine sulcus. In the unfolded cortical surface it can be seen that the two clusters over the anatomical image really are the V1 response and the response in V2, close to the border

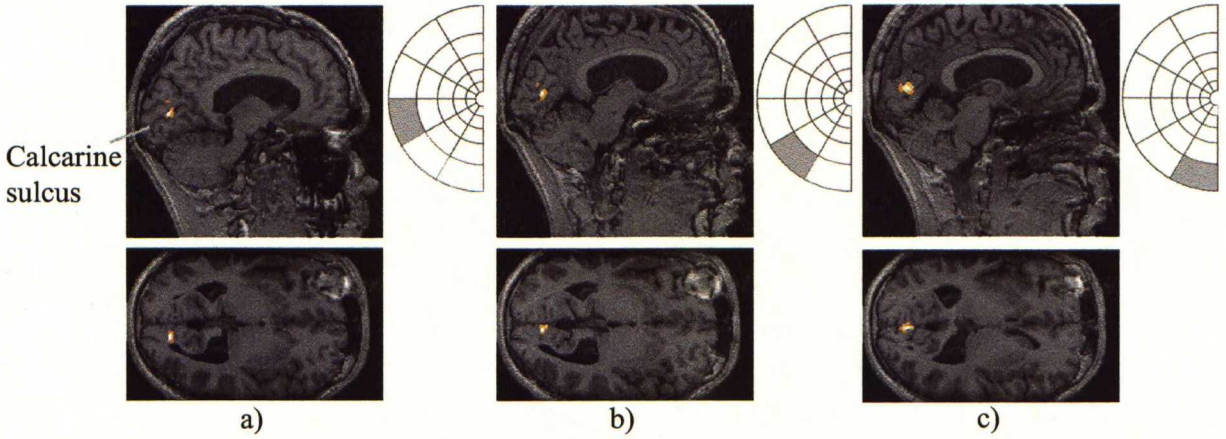


Figure 7.1: *Example activation patterns for subject VR (k number of voxels in a cluster, T^{max} maximum T value in the cluster). The activations are thresholded at $p_{FWE} < 0.05$. a) As a response for stimulation of a visual field region in the left hemifield just below the horizontal meridian, two clusters ($k_1=20$, $T_1^{max}=18.66$, $k_2=21$, $T_2^{max}=12.43$) are seen in the right occipital cortex. b) Likewise, the stimulation of region in the lower visual field evokes response, which can be seen as two clusters ($k_1=18$, $T_1^{max}=17$, $k_2=8$, $T_2^{max}=7.76$). c) One cluster ($k=22$, $T^{max}=15.04$) above the calcarine sulcus is seen as a response to the stimulation of a visual field regions next to lower vertical meridian.*

between areas V2 and VP, as expected according to the visual field location. Fig. 7.3 shows all the assigned activation patterns for stimulation of one hemifield for subject LS.

As a summary of the surface oriented results, for all the subject all the 60 stimulated visual field regions produce statistically significant response in V1. Approximately 42% of activations are also present in visual area V2/V3.

7.3 MffMRI Grid on Reconstructed Surface

To simultaneously visualize results from the multifocal paradigm, an mffMRI grid was implemented. In this grid, the mean locations of local V1 activations are connected on the reconstructed cortical surface. The implementation of the Matlab function producing mffMRI grids is described in Appendix A.1. The mffMRI grids for all the subjects are shown in Fig. 7.4. The grids are shown over the polar data from the phase-encoded retinotopic mapping.

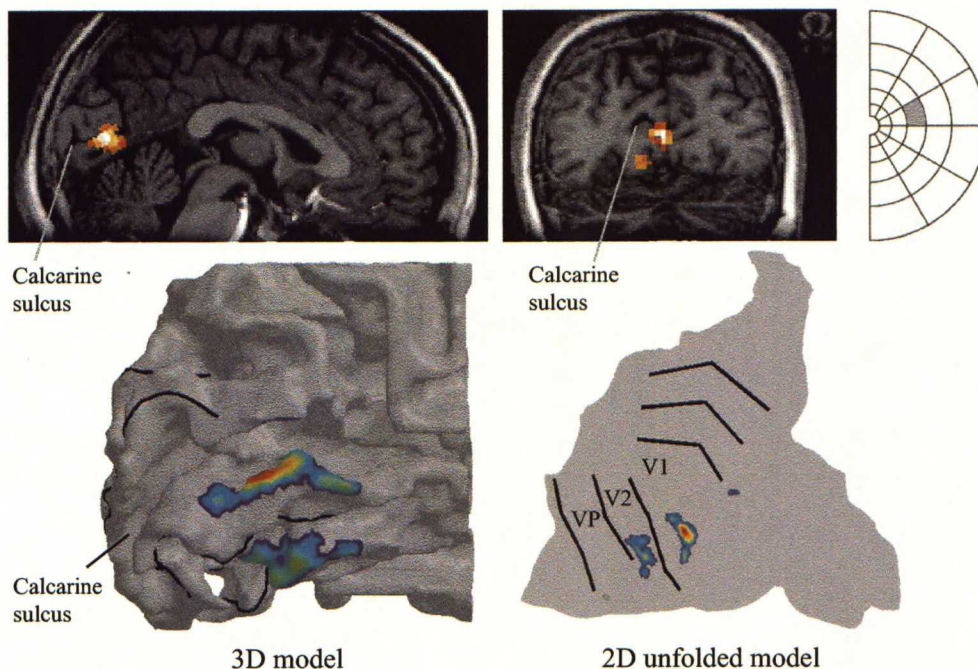


Figure 7.2: *Statistically significant response ($p_{FWE} < 0.05$, two active clusters: $k_1=83$, $T_1^{max}=30.3$, $k_2=13$, $T_2^{max}=8.3$) on the anatomical image of subject MU, assigned to the reconstructed left occipital cortex and in the unfolded cortical surface. The borders between visual areas V1, V2 and V3/VP are mapped with phase-encoded approach. The stimulated visual field region was in the right hemifield just above the horizontal meridian.*

The mffMRI grids produce clear retinotopic maps for each subject's both hemifields. There are obvious differences between the mffMRI grids of the subjects and these mffMRI grids could be used to evaluate the inhomogeneities and individual differences of the visual field representation in V1.

There are still some problems with the mffMRI grids. For some subjects the grids are somewhat distorted, as for example the mffMRI grid on the left hemisphere of subject SV in Fig. 7.4. But, it appears that these problems arise from the errors in the segmentations, because the phase-encoded representations appears to be distorted as well (see for example the left hemisphere of subject VR in Fig. 7.4)

Table 7.1 contains measurements of the cortical areas of V1 representing the visual field between 1.7° - 10.4° for all the subjects. The surface areas are calculated using Heron's formula (Eq. 6.15) from the mffMRI grids. The areas of the right and left as well as of ventral and dorsal divisions are shown separately. V1 in the left hemisphere (mean 1600 mm^2 , standard deviation 538 mm^2) appears to be

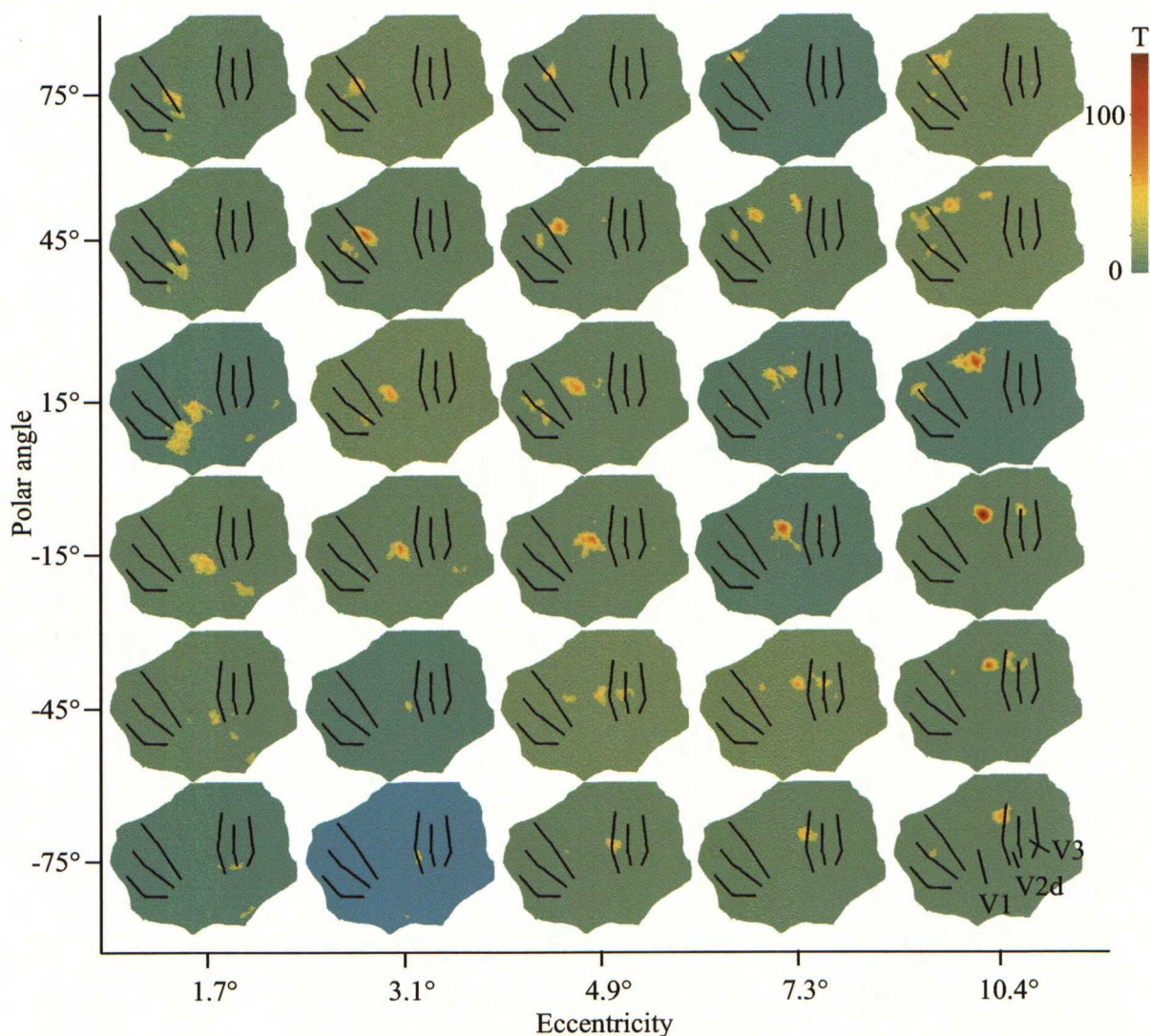


Figure 7.3: *Projected activation patterns for stimulation of the left hemifield, shown in the unfolded right occipital cortex of the subject LS. The T values were smoothed along the cortical surface and activations were thresholded at $T = 10$. The eccentricity of the stimulated visual field region increases from left to right and the polar angle from down to top (see also Fig. 6.1). As a reference, the borders between visual areas mapped with phase-encoded approach are shown. The topography of the multifocal responses follow the retinopic visual field representation in the visual areas. All 30 stimulated areas evoke a response in V1 or in the border between visual areas V1 and V2 and 17 visual field areas also in V2 or in the border between areas V2 and V3/VP.*

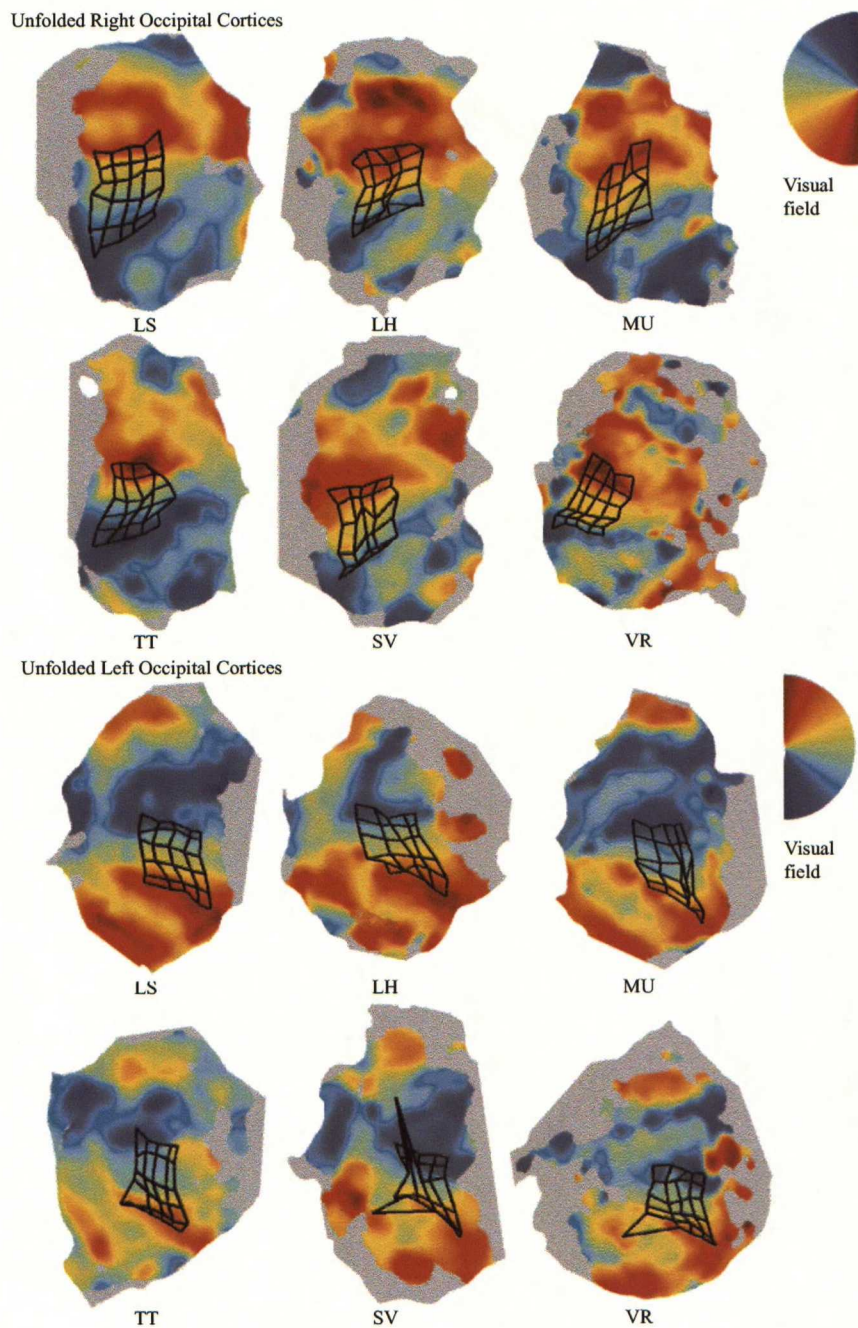


Figure 7.4: The mffMRI grids shown for all the six subjects over the unfolded cortical surfaces. The initials of the subjects are shown below the pictures. The colors code the polar angle of the visual field, mapped with the phase-encoded retinotopic approach.

Table 7.1: *The surface areas of V1 between 1.7° and 10.4° eccentricities calculated from the mffMRI grids for all six subjects.*

Subject	Hemisphere	Ventral V1 (mm ²)	Dorsal V1 (mm ²)	Total V1 (mm ²)
LS	left	630	589	1219
	right	781	672	1453
LH	left	753	785	1538
	right	870	878	1748
MU	left	495	747	1242
	right	663	900	1563
TT	left	501	631	1132
	right	516	556	1072
SV	left	831	1139	1970
	right	432	579	1011
VR	left	1795	706	2501
	right	455	884	1339
mean	left	834	766	1600
	right	620	745	1365
	left+right	727	756	1482

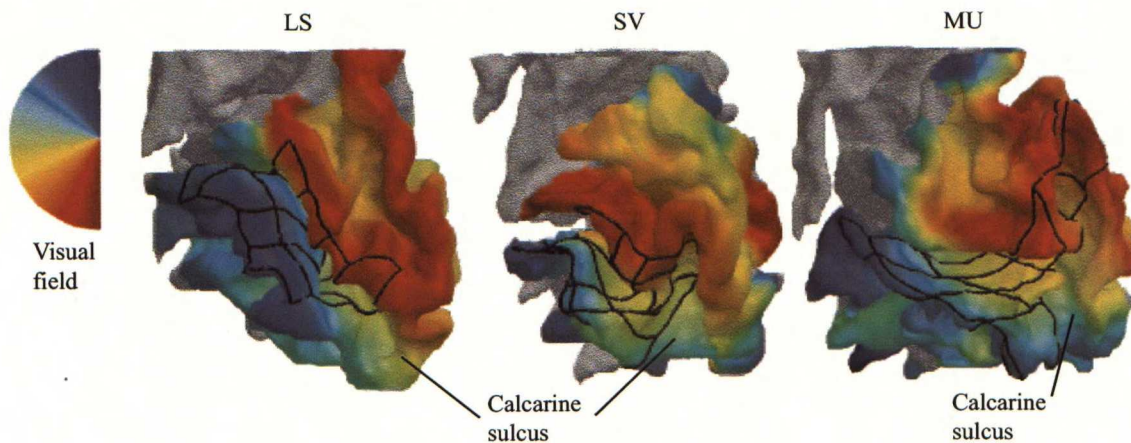


Figure 7.5: *Examples of individual variability in the shape of the calcarine sulcus and in the location of V1. Polar data from phase-encoded retinotopic mapping overlaid with the mffMRI grid are shown for right occipital cortices of subjects LS, SV and MU.*

somewhat larger than V1 in the right hemisphere (mean 1365 mm^2 , standard deviation 285 mm^2). As well, there are some differences in the surface areas between dorsal division of V1 (mean 756 mm^2 , standard deviation 538 mm^2) and the ventral division (mean 727 mm^2 , standard deviation 172 mm^2). But for this small group of subjects the differences are not statistically significant. With Wilcoxon signed rank test of equality of medians, the significance probability for left versus right hemisphere is $p = 0.8438$ and for dorsal versus ventral division $p = 0.6875$. However, this result is strongly limited due to inaccuracies of the segmentation and thus we need further improvement in anatomical segmentation methods.

V1 is always located near the calcarine sulcus, but there is significant variation in the location of V1 in relation to this sulcus, as well as in the size of V1 between individuals. As an example, the mffMRI grids for three subjects and the polar data from phase-encoded retinotopic mapping are shown over the reconstructed cortices of the right hemispheres in Fig. 7.5. There are significant differences between the shapes of the calcarine sulci between these subjects. Not only the positions but also the sizes of visual areas vary between subjects. The cortical surface of V1 in right hemisphere for the subject MU is roughly 1.5 times the surface area of right V1 for the subject SV.

Table 7.2: *Estimated parameters a and k of log map model for both hemispheres for all the subjects. The mean values and RMS error terms are also shown. In subject LH, the mffMRI grids representing the multifocal activations do not appear to converge towards fovea in these eccentricities, and therefore the parameter a fall to the minimum value of 0.001.*

Subject	Hemisphere	k	a	RMS error
LS	left	13.6	0.295	3.8727
	right	16.1	0.440	3.9988
LH	left	15.4	0.001	5.8890
	right	15.1	0.001	4.6233
MU	left	16.9	0.775	5.3869
	right	17.5	0.855	5.8294
TT	left	16.8	0.818	4.2532
	right	13.0	0.205	3.8339
SV	left	13.0	0.185	4.6331
	right	14.5	0.748	3.9881
VR	left	12.2	0.001	3.6221
	right	15.9	0.477	2.9728
mean	left	14.7	0.346	
	right	15.4	0.454	
	left+right	15.0	0.400	

7.4 Application of Log Map Model to mffMRI Data

The mapping of the visual field to cortical surface can be modeled with a complex logarithm conformal function $w = k \cdot \ln(z + a)$ (Eq. 2.4). Parameters a and k in this mapping function are now estimated from the multifocal activation patterns (see description of the implementation of this optimization from Appendix A.3). In Table 7.2 are the estimated parameters and root-mean-square (RMS) errors for each subjects' both hemispheres and the mean values.

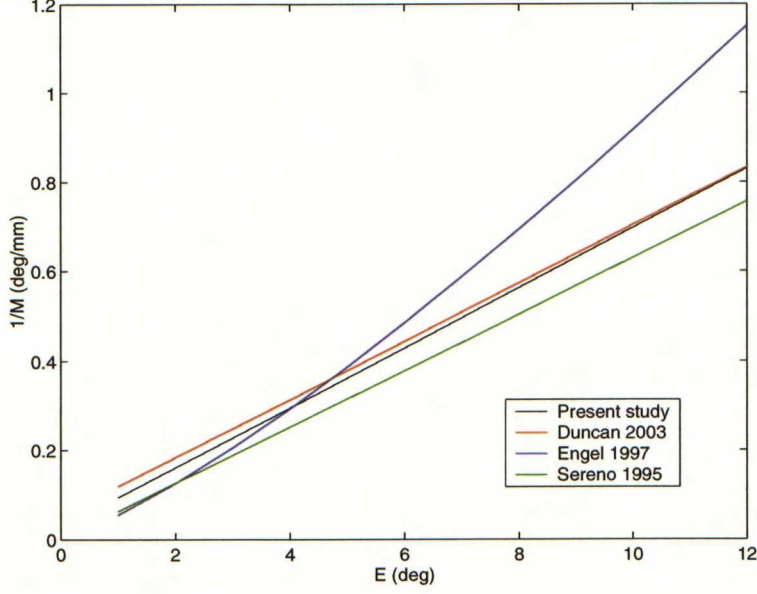


Figure 7.6: *Our estimate of inverse cortical magnification ($1/M$) as a function of eccentricity E ($1^\circ - 12^\circ$), plotted alongside with estimates of $1/M$ from previous fMRI studies [20, 24, 26].*

There is variation in the a and k values between subjects. In the optimization of these parameters, some outliers nodes in the mfmMRI grids were excluded from the optimization.

An estimate for the human cortical magnification can be calculated from our data, based on estimates of a and k , and using formula 2.7

$$M = \left| \frac{k}{z + a} \right| = \left| \frac{15}{z + 0.4} \right|. \quad (7.1)$$

Usually, the linear relationship between $1/M$ and eccentricity (E) is presented as

$$1/M = \left| \frac{z + a}{k} \right| = \left| \frac{z + 0.4}{15} \right| \simeq 0.067E + 0.027. \quad (7.2)$$

In Fig. 7.6, our estimate of $1/M$ is plotted as function of E together with results from previous studies (see Eqs. 2.1-2.3).

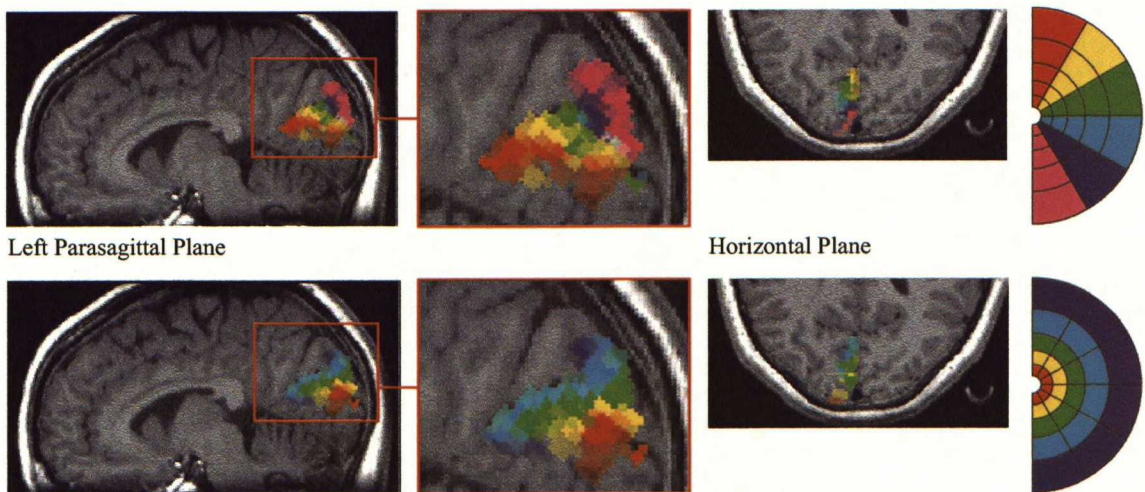


Figure 7.7: V1 clusters for right hemifield stimulation of subject LH are presented on top of the anatomical image. In the upper row, the colors code the polar angle and in the lower row the eccentricity of the visual field. The retinotopic organization is clearly seen. Upper visual field is represented below and lower visual field above the calcarine sulcus. The foveal visual field regions are represented in the occipital pole and the more peripheral parts near the parieto-occipital sulcus.

7.5 Localization of V1

Surface oriented analysis is not necessary to take advantage of the multifocal data. The segmentation of subject's cortical surface still needs manual work and therefore the surface oriented analysis is not yet a suitable clinical tool or a tool for wider study in population. Therefore, it is important that the multifocal results can be analyzed qualitatively also in 3D. A 3D display function for multifocal data was created, based on existing SPM2 functions (see Appendix A.2).

Fig. 7.7 shows the multifocal results for stimulation of right hemifield over anatomical image. In this figure, only the cluster with the maximum T value are included for each visual field region. With the present multifocal stimulus, the statistically strongest responses emerge in V1. In consequence, the active clusters define the position of V1 representing visual field 1° - 12° .

In the 3D display of multifocal results, the colors code either the polar angle or eccentricity of the visual field to reveal the retinotopic visual field representation. With a better signal-to-noise ratio in V2 and V3, it could be possible to include these areas also in the 3D display. The whole V1, not to mention V2/V3, is not possible to visualize with a single anatomical slice, as for example in Fig. 7.7, but

the advantage of the mffMRI 3D display together with SPM2 tools is that different slices can be browsed to perceive the overall structure of the visual areas.

7.6 Reproducibility of Measurements

To study the reproducibility of the multifocal measurements the measurement session was repeated for two subjects. In Fig. 7.8, results are shown from two sessions for the subject LH. The statistical results can be well repeated, though the cluster sizes and the maxima of the T value do vary between measurements. The localization of V1 from the MR images can be well repeated (see upper row in Fig. 7.8). The mffMRI grids in the unfolded cortical surfaces also look roughly similar but there are some differences in the node locations. These differences are probably due to errors in the coregistration of the functional data to the structural image.

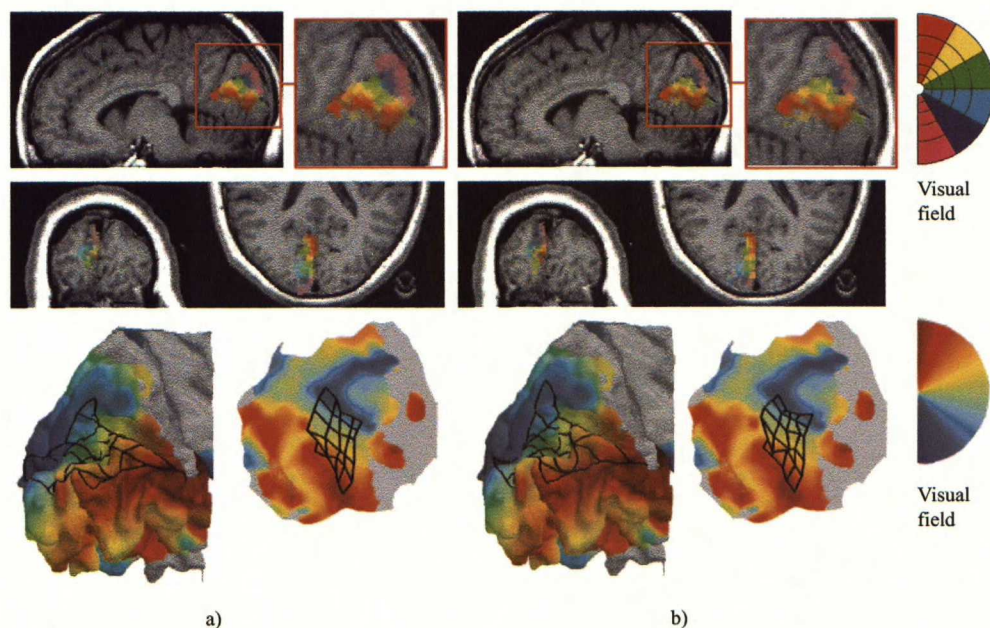


Figure 7.8: The active V1 clusters in left hemisphere over anatomical image and the mffMRI grid in the reconstructed left occipital cortex from a) the first measurement and from b) the repeated measurement for the subject LH. The active clusters over the anatomical images are thresholded similarly ($p_{FWE} < 0.05$) and shown over the same structural image slices. As reference, the polar data from phase-encoded retinotopic mapping is shown with the mffMRI grid on the reconstructed cortex.

Chapter 8

Discussion

8.1 On Results

With mffMRI the local visual field representation in the visual cortex can be studied with excellent spatial resolution. For all the subjects, all 60 visual field regions in the multifocal stimulus evoked statistically significant responses in V1 and approximately 42% of responses were also observed in V2 or in V3. In the surface oriented analysis, an mffMRI grid was developed to illustrate local anisotropies. From mffMRI grids, the surface areas of V1 were calculated. There are significant differences in surface areas between subjects. In addition, the surface area of left V1 (mean 1600 mm^2) appears to be somewhat larger than the surface area of right V1 (mean 1365 mm^2). Similar findings have also been reported in previous studies [59].

The log-polar conformal mapping technique of visual field representation in cortical surface does not fit very well to the multifocal activation patterns. There is a lot of variability in the optimized a and k parameter values between subjects. The parameter k is an overall scaling factor and a reflects the proportion of V1 devoted to central vision. The mean value of our estimate of a is 0.4. In previous studies, the measurements of a have varied on humans from 0.7° to 1.5° [60, 26]. A large variation in the estimates of a was also reported in these studies.

The RMS errors in the fitting of the log-map model grids to the mffMRI grids are quite large. Some distortions of distances and angles are induced in the unfolding of the reconstructed cortical surface [3]. This distorts to certain amount also the node locations in the mffMRI grid representing multifocal activations and therefore also the distances between activations. Besides, errors in segmentation of the structural

data distort mffMRI grids. Another possibility is that stimulated visual field region with the smallest eccentricity (mean 1.7°) is already too far from the fovea and the grid does not converge enough for the optimization of parameter a to success.

The log-map model, being a conformal mapping function, might not be optimal to represent the projection of visual field to human cortical surface. The use of conformal mapping implies that the retinotopic mapping of visual field is isotropic, although there may be important anisotropies in the visual field representations. A quasiconformal mapping technique with a constant rotational shear (wedge mapping) has been introduced to cover the reported anisotropy near the border of areas V1 and V2 and to unify areas V1, V2 and V3 into a single complex [61]. But neither can this model explain the inhomogeneities in the mffMRI grids. It could be beneficial to make an attempt to construct a better fitting model based on the existing models.

Not many precise estimates of cortical magnification on human have yet been made using fMRI [18, 20, 24, 26, 62]. Most of these estimates have been presented based on phase-encoded retinotopic data [18, 20, 24, 62]. But because the phase-encoded stimulus wraps around from periphery to fovea, the temporal phase is difficult to estimate in these regions and the measure of the cortical magnification is disturbed [26].

In one fMRI study, stationary flickering annuli were used together with conformal mapping technique to estimate human cortical magnification [26]. But compared to the present study, the activations to flickering annuli are much more imprecise than our discrete multifocal activation patterns. Nevertheless, mffMRI has potential for accurate estimation of human cortical magnification.

To study the reproducibility of the multifocal responses, the multifocal measurement session was repeated on two subjects (LH and SV). The repeated measurements demonstrated that the volume-based responses are well reproducible. Though, there is some variation in the strength of the activations and in the amount of voxels in clusters. This is not surprising, because it has been reported that the evoked hemodynamic responses can vary within a single subject from one day to another [38]. In addition, measurement noise and small errors in coregistration of functional and anatomical images explain partially the differences. Nevertheless, the 3D analysis and localization of V1 from MR image is well reproducible.

Surface oriented analysis is very sensitive to errors in coregistration of functional and anatomical data. The mffMRI grid from the repeated measurement look only roughly similar to the mffMRI grid from the first measurement. It is also possible that the viewing distance to the stimulus was not exactly the same in the measurements. A change in viewing distance alters the stimulated visual field

regions and therefore the activations are not located exactly similarly.

8.2 Applications in Basic Research

Multifocal fMRI has potential for wide basic research and clinical use. In future, the multifocal paradigm will be introduced to MEG as well. Our plan is to stimulate the same visual field regions as in mffMRI and combine the results. From surface oriented mffMRI results, a priori information about the position and orientation of the active loci can be seeded to the MEG analysis [47]. Then, timing of the activations can be studied with MEG with excellent temporal resolution. However, the residual variance in the MEG after strong a priori model must be explained with traditional inverse solution algorithms, or attenuated by other means. Otherwise, they interfere with source amplitudes of the a priori dipoles.

Multifocal paradigm could even be adapted to map other parametric spaces than retinotopic organization of visual field in the cortex. In principle, the whole cortex can be parametrically coded, and it is just the question of finding the right parameters. Already in V1, orientation preference, spatial frequency and ocular dominance are coded in neighboring columns of neurons, but the resolution of fMRI is not yet sufficient to map these columnar organizations in humans.

8.3 Applications in Clinical Medicine

The data analysis of mffMRI data is straightforward and the SPM2 statistical analysis of the multifocal data can be even fully automated. The volume-based analysis is reliable and the multifocal responses reproducible. Thus, mffMRI is a suitable tool for clinical medicine. With mffMRI, V1 can be localized rapidly and accurately. This could be useful for example in the presurgical evaluation of V1 position, where V1 is localized so that it can be avoided in an operation.

For retinotopic mapping, the mffMRI is a more straightforward method than phase-encoded approach. There is no need for Fourier analysis and the retinotopic organization can already be visualized in volume-based analysis. With mffMRI responses, it would be even possible to follow the plastic changes in the retinotopically organized visual areas. In addition, mffMRI offers objective perimetry, which could be used to detect small lesions in the retinocortical pathway. Compared to mfVEP, mffMRI has no cancellation of signals close to horizontal meridian.

8.4 Limitations of mffMRI

With the current stimulation setup, the stimulated visual field is limited to eccentricities $1^\circ - 12^\circ$. Compared to mfVEP where the stimulus can extend far to the visual periphery, in mffMRI the narrow bore of the magnet limits the visual field. To study retinotopic organization in higher-order visual areas, for example in V6, it would be important to stimulate larger visual field regions and also regions further in periphery than what is possible with the current multifocal measurement setup. One possibility would be to bring the back-projection screen very close to subject and correct refraction with glasses.

At the moment, the largest problems with the mffMRI relate to lack of robust segmentation algorithm and imperfect coregistration of anatomical and functional series. Both of these add uncertainty to surface oriented analysis. Because of the errors in the segmentations, the mffMRI grids are for some subjects somewhat distorted and this distorts the calculations of the surface areas and fitting of the log-polar map. In addition, segmentation needs a lot of manual work. With the present tools, surface oriented analysis is not a suitable tool for larger study in population.

8.5 Conclusions and Future Development

The results with mffMRI are promising; the visual field representation in the human cortex can be studied with high sensitivity. One study has been previously published, where visual stimulation with m-sequence was used in fMRI, but in that study only two regions in the visual field were stimulated and the study concentrated on the nonlinearity of the responses [63]. At the moment, besides our research group several other groups are developing mffMRI, but they use m-sequence stimulation and have divided the visual field only into four or nine regions [64, 65]. In addition, a research group at the University of California, Berkeley, is working on mffMRI with 24 visual field regions. Compared to our study, this study has not proceeded to surface oriented analysis. Hence the group does not, for example, have the possibility to estimate the human cortical magnification.

In future, the attempt in our research group is to enhance V2 and V3 responses. In other laboratories the use of colored stimuli has been observed useful; the luminance contrast is sacrificed in favor of color contrast and V2/V3 responses are enhanced compared to V1 responses. It could also be beneficial to stimulate larger visual field areas. Because the receptive field sizes in V2 and V3 are already larger

than in V1, it is possible that in V2/V3 cortical representations of neighboring visual field regions overlap in the current multifocal stimulus. Then the signals are correlated and can not be identified from the data. For the same reason, it should be tried, whether increasing the space between stimulated areas enhances the signals.

It would also be useful to include fovea (visual field $<1^\circ$) as a single stimulated region to the multifocal stimulus. This is necessary for preoperative V1 mapping, because central V1 is of paramount importance for vision.

Bibliography

- [1] E.E. Sutter. Imaging visual function with the multifocal m-sequence technique. *Vision Research*, 41:1241–1255, 2001.
- [2] A.C. James. The pattern-pulse multifocal visual evoked potential. *IOVS*, 44:879–890, 2003.
- [3] J. Warnking, A. Guérin-Dugué, C. Delon-Martin, S. Olympieff, N. Richard, A. Chéhikian, and C. Segebarth. fMRI retinotopic mapping - step by step. *NeuroImage*, 17:1665–1683, 2002.
- [4] D. Purves, G.J. Augustine, D. Fitzpatrick, L.C. Katz, A.-S. LaMantia, J.G. McNamara, and S.M. Williams, editors. *Neuroscience*. Sinauer Associates, 2001.
- [5] C.A. Curcio and K.A. Allen. Topography of ganglion cells in human retina. *J. Comp. Neurol.*, 300:5–25, 1990.
- [6] S.H. Hendry and R.C. Reid. The koniocellular pathway in primate vision. *Annu. Rev. Neurosci.*, 23:127–53, 2000.
- [7] L.G. Nowak and J. Bullier. The timing of information transfer in the visual system. In K.S. Rockland, J.H. Kaas, and A. Peters, editors, *Cerebral Cortex*, pages 205–241. Plenum Press, 1997.
- [8] R.B.H. Tootell, A.M. Dale, M.I. Sereno, and R. Malach. New images from human visual cortex. *TINS*, 19:481–489, 1996.
- [9] D.J. Felleman and D.C. Van Essen. Distributed hierarchical processing in the primate cerebral cortex. *Cerebral Cortex*, 1:1–47, 1991.
- [10] D.C. Van Essen. Organization of visual areas in macaque and human cerebral cortex. In L. Chalupa and J.S. Werner, editors, *The Visual Neurosciences*, pages 507–521. MIT Press, 2004.

- [11] J. Bullier. Hierarchies of cortical areas. In J.H. Kaas and C.E. Collins, editors, *The Primate Visual System*, pages 181–204. CRC Press, 2004.
- [12] J.H. Kaas. Early visual areas: V1, V2 V3, DM, DL, and MT. In J.H. Kaas and C.E. Collins, editors, *The Primate Visual System*, pages 139–159. CRC Press, 2004.
- [13] K. Grill-Spector. The neural basis of object perception. *Curr Opin Neurobiol*, 13:159–166, 2003.
- [14] G. Rizzolatti and M. Matelli. Two different streams from the dorsal visual system: anatomy and function. *Exp Brain Res*, 153:146–157, 2003.
- [15] J. Bullier. An integrated model of visual processing. *Brain Research Reviews*, 36:96–107, 2001.
- [16] S. Vanni. Näkötiedon käsittelyn aivomekanismit. *Duodecim*, 2004 (In Press).
- [17] J.C. Horton and W.F. Hoyt. The representation of the visual field in human striate cortex. *Arch Ophthalmol*, 109:816–824, 1991.
- [18] S.A. Engel, D.E. Rumelhart, B.A. Wandell, A.T. Lee, G.H. Lee, E.-J. Chichilnisky, and M.N. Shadlen. fMRI measurements of human visual cortex. *Nature*, 369:525, 1994.
- [19] E.A. DeYoe, G.J. Carman, P. Bandettini, S. Glickman, J. Wieser, R. Cox, D. Miller, and J. Neitz. Mapping striate and extrastriate visual areas in human cerebral cortex. *Proc. Natl. Acad. Sci. USA*, 93:2382–2386, 1996.
- [20] S.A. Engel, G.H. Glover, and B.A. Wandell. Retinotopic organization in human visual cortex and the spatial precision of functional MRI. *Cereb. Cortex*, 7:181–192, 1997.
- [21] T.M. Preuss. Specializations of the human visual system: The monkey model meets human reality. In J.H. Kaas and C.E. Collins, editors, *The Primate Visual System*, pages 231–259. CRC Press, 2004.
- [22] D.L. Sheinberg and N.K. Logothetis. The role of temporal cortical areas in perceptual organization. *Proc. Natl. Acad. Sci. USA*, 94:3408–3413, 1997.
- [23] A.W. Roe. Modular complexity of area V2 in the macaque monkey. In J.H. Kaas and C.E. Collins, editors, *The Primate Visual System*, pages 109–138. CRC Press, 2004.

- [24] M.I. Sereno, A.M. Dale, J.B. Reppas, K.K. Kwong, J.W. Belliveau, T.J. Brady, B.R. Rosen, and R.B.H. Tootell. Borders of multiple visual areas in humans revealed by functional magnetic resonance imaging. *Science*, 268:889–893, 1995.
- [25] M. Daniel and D. Whitteridge. The representation of the visual field on the cerebral cortex in monkeys. *J. Physiol.*, 159:203–221, 1961.
- [26] R. O. Duncan and G. M. Boynton. Cortical magnification within human primary visual cortex correlates with acuity thresholds. *Neuron*, 38:659–671, 2003.
- [27] E.L. Schwartz. Computational anatomy and functional architecture of striate cortex: a spatial mapping approach to perceptual coding. *Vision Research*, 20:645–669, 1980.
- [28] E.L. Schwartz. Computational studies of the spatial architecture of primate visual cortex. In A. Peters and K.S. Rockland, editors, *Cerebral Cortex*, pages 359–411. Plenum Press, 1994.
- [29] E.M. Haacke, R.W. Brown, M.R. Thompson, and R. Venkatesan. *Magnetic Resonance Imaging: Physical Principles and Sequence Design*. Wiley-Liss, 1999.
- [30] J.P. Hornak. *The Basics of MRI*. 1996-2003. <http://www.cis.rit.edu/htbooks/mri/index.html>, 25.9.2003.
- [31] R.B. Buxton. *Introduction to Functional Magnetic Resonance Imaging*. Cambridge University Press, 2002.
- [32] M.S. Cohen. Echo-planar imaging and functional MRI. In C.T.W. Moonen and P.A. Bandettini, editors, *Functional MRI*, pages 137–148. Springer, 1999.
- [33] A. Villringer. Physiological changes during brain activation. In C.T.W. Moonen and P.A. Bandettini, editors, *Functional MRI*. Springer, 1999.
- [34] W. Chen and S. Ogawa. Principles of BOLD functional MRI. In C.T.W. Moonen and P.A. Bandettini, editors, *Functional MRI*. Springer, 1999.
- [35] K.J. Friston, E. Zarahn, O. Joseph, R.N.A. Henson, and A.M. Dale. Stochastic designs in event-related fMRI. *NeuroImage*, 10:607–619, 1999.
- [36] G.K. Aguirre and M.D’Esposito. Experimental design for brain fMRI. In C.T.W. Moonen and P.A. Bandettini, editors, *Functional MRI*. Springer, 1999.

- [37] R.L. Buckner and T.S. Braver. Event-related functional MRI. In C.T.W. Moonen and P.A. Bandettini, editors, *Functional MRI*. Springer, 1999.
- [38] G.K. Aguirre, E. Zarahn, and M.D'Esposito. The variability of human, BOLD hemodynamic responses. *NeuroImage*, 8:360–369, 1998.
- [39] D.L. Scacter, R.L. Buckner, W. Koutstaal, A.M. Dale, and B.R. Rosen. Late onset of anterior prefrontal activity during true and false recognition: An event-related fMRI study. *NeuroImage*, 6:259–269, 1997.
- [40] S.E. Dumoulin, R.D. Hoge, C.L. Baker Jr., R.F. Hess, R.L. Achtman, and A.C. Evans. Automatic volumetric segmentation of human visual retinotopic cortex. *NeuroImage*, 18:576–587, 2003.
- [41] E.E. Sutter. The fast m-trasform: a fast computation of cross-correlation with binary m-sequences. *Soc Ind Appl Math*, 20:686–694, 1991.
- [42] H.A. Baseler and E.E. Sutter. M and P components of the VEP and their visual field distribution. *Vision Research*, 37:675–690, 1997.
- [43] E.E. Sutter and D. Tran. The field topography of ERG components in man – I. the photopic luminance response. *Vision Research*, 32:433–46, 1992.
- [44] S.D. Slotnick, S.A. Klein, T. Carney, E. Sutter, and Shahram Dastmalchi. Using multi-stimulus VEP source localization to obtain a retinotopic map of human primary visual cortex. *Clinical Neurophysiology*, 110:1793–1800, 1999.
- [45] D.C. Hood, J.G. Odel, and X. Zhang. Tracking the recovery of local optic nerve function after optic neuritis: a multifocal VEP study. *IOVS*, 41:4032–4038, 2000.
- [46] A. Klistorner and S.L. Graham. Objective perimetry in glaucoma. *Ophthalmology*, 107:2283–2299, 2000.
- [47] S. Vanni, J. Warnking, M. Dojat, C. Delon-Martin, J. Bullier, and C. Segebarth. Sequence of pattern onset responses in the human visual areas: an fMRI constrained VEP source analysis. *NeuroImage*, 21:801–817, 2004.
- [48] S. Vanni, M. Dojat, J. Warnking, C. Delon-Martin, C. Segebarth, and J. Bullier. Timing of interactions across the visual field in the human cortex. *NeuroImage*, 21:818–828, 2004.
- [49] Statistical parametric mapping. <http://www.fil.ion.ucl.ac.uk/spm/>, 18.2.2004.

- [50] Piia Häkkinen. Magneettivuon tiheyden mittausmenetelmän kehittäminen kolmen teslan magneettikuvauslaitteeseen. Master's thesis, Helsinki University of Technology, 2004.
- [51] K.J. Friston. Statistical parametric maps in functional imaging: A general linear approach. *Hum. Brain Mapp.*, 2:189–210, 1995.
- [52] R. Henson. Analysis of fMRI timeseries: Linear time-invariant models, event-related fMRI and optimal experimental design. In R.S.J. Frackowiak, editor, *Human Brain Function*, chapter 10. Academic Press, second edition, 2004.
- [53] K.J. Friston, W. Penny, C. Phillips, S. Kiebel, G. Hinton, and J. Ashburner. Classical and bayesian inference in neuroimaging: Theory. *NeuroImage*, 16:465–483, 2002.
- [54] K. J. Friston, D. E. Glaser, R. N. A. Henson, S. Kiebel and C. Phillips, and J. Ashburner. Classical and bayesian inference in neuroimaging: Applications. *NeuroImage*, 16:484–512, 2002.
- [55] N. Lange. Statistical procedures for functional MRI. In C.T.W. Moonen and P.A. Bandettini, editors, *Functional MRI*. Springer, 1999.
- [56] M. Brett, W. Penny, and Kiebel. An introduction to random field theory. In R.S.J. Frackowiak, editor, *Human Brain Function*, chapter 14. Academic Press, second edition, 2004.
- [57] K.J. Worsley, S. Marrett, P. Neelin, A.C. Vandal, K.J. Friston, and A.C. Evans. A unified statistical approach for determining significant signals in images of cerebral activation. *Human Brain Mapping*, 4:58–73, 1996.
- [58] D. Yekutieli and Y. Benjaminini. Resampling-based false discovery rate controlling multiple test procedures for correlated test statistics. *Journal of Statistical Planning and Inference*, 82:171–196, 1999.
- [59] R.F. Dougherty, V.M. Koch, A.A. Brewer, B. Fischer, J. Modersitzki, and B.A. Wandell. Visual field representation and locations of visual areas V1/2/3 in human visual cortex. *Journal of Vision*, 3:586–598, 2003.
- [60] S. Endo, H. Toyama, Y. Kimura, K. Ishii, M. Senda, M. Kiyosawa, and A. Uchiyama. Mapping visual field with positron emission tomography by mathematical modeling of the retinotopic organization in the calcarine cortex. *IEEE Transactions on Medical Imaging*, 16:252–260, 1997.

- [61] M. Balasubramanian, J. Polimeni, and E.L. Schwartz. The V1-V2-V3 complex: quasiconformal dipole maps in primate striate and extra-striate cortex. *Neural Networks*, 15:1157–1163, 2002.
- [62] A.T. Smith, K.D. Singh, A.L. Williams, and M.W. Greenlee. Estimating receptive field size from fMRI data in human striate and extrastriate visual cortex. *Cereb. Cortex*, 11:1182–1190, 2001.
- [63] P. Kellman, P. van Gelderen, J.A. de Zwart, and J.H. Duyn. Method for functional MRI mapping of nonlinear response. *NeuroImage*, 19:190–199, 2003.
- [64] B.L. Foster, D.P. Crewther, and S.G. Crewther. Efficient retinotopic mapping of occipital cortex through application of a multi-focal paradigm to fMRI. Abstract presented as a poster at the 10th International Conference on Human Brain Mapping (HBM 2004) held in Budapest, Hungary, June 13-17, 2004.
- [65] M. Fukunaga, P. van Gelderen, J.A. de Zwart, M. Jansma, and J.H. Duyn. Retinotopic fMRI mapping with pseudo-random stimulus presentation using the m-sequence paradigm. Abstract presented as a poster at the 10th International Conference on Human Brain Mapping (HBM 2004) held in Budapest, Hungary, June 13-17, 2004.
- [66] K.S. Arun, T.S. Huang, and S.D. Blostein. Least-squares fitting of two 3-D point sets. *IEEE Transactions on Pattern Analysis and Machine Intelligence*, 9:698 – 700, 1987.

Appendix A

Implementations

A.1 MffMRI Grid

The mffMRI grid is implemented in *mffmri_grid.m* –Matlab function. One grid consists of 30 nodes which are the mean V1 activations corresponding to stimulation of one hemifield (30 visual field regions) with multifocal stimulus. The locations of these activations are searched with a locally developed dipole extraction function which searches from fMRI activations assigned to the reconstructed cortex a priori dipoles to MEG analysis. To search the location of an activation, T value and cluster size thresholds are defined.

In constructing the mffMRI grid, first the most foveal activations are located using cluster size threshold of 5 voxels and T value threshold of 0.4 times the maximum T value of the activation in question. If no active cluster is found with these thresholds, the T value threshold is reduced with steps of 0.1 times the maximum T value until at least one active cluster is found. If more than one active cluster is found, the strongest activation is chosen to be connected along the cortical surface with activations representing the neighboring visual field locations. This procedure is repeated to all eccentricities (see Fig. A.1d). Then localized activations are connected along equal polarity directions (see Fig. A.1e).

With our multifocal stimulus, the strongest activation is almost always in V1, but in some cases stronger responses can be evoked from V2 or V3 (see an example in A.1e). The next step in constructing the mffMRI grid is to exclude these positively wrong nodes from the grid. To implement this, the mean distance from a node to the neighboring node and the standard deviation of the mean distance between nodes are calculated. If the deviation of the mean distance from

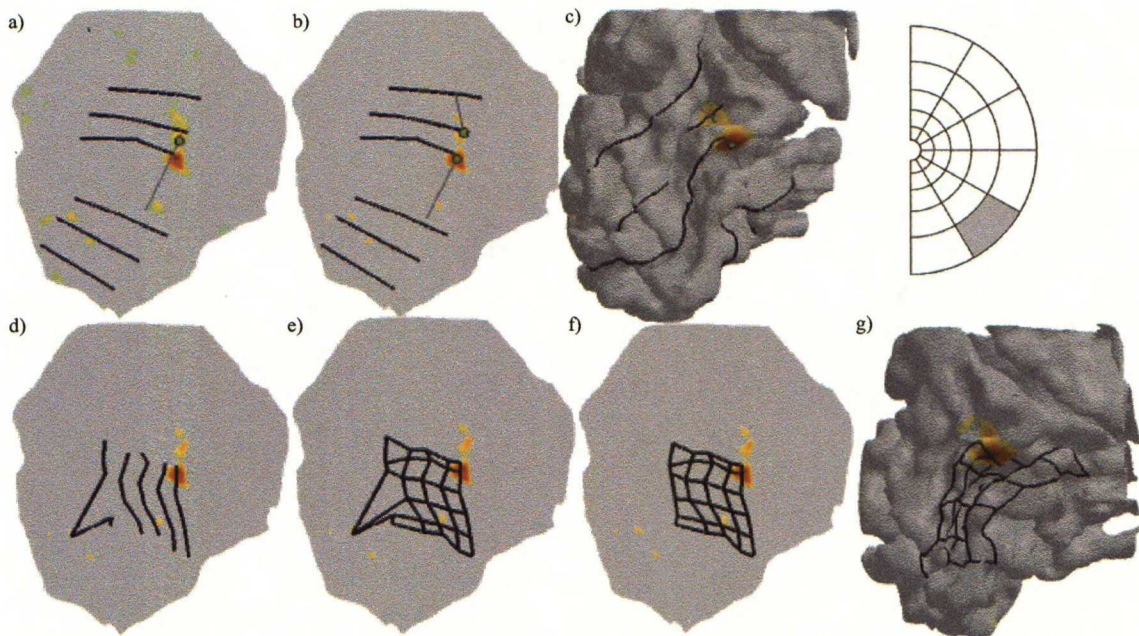


Figure A.1: *Constructing an mffMRI grid and an example activation pattern (the stimulated visual field region in the multifocal stimulus is shown on the right hand side) a) When a T value threshold of 5 and cluster size threshold of 5 voxels were used the visual field region representations in V1 and V2 are clustered together. b) When the T value threshold is elevated to 10, the V1 and V2 activations are split into two active clusters. c) The a priori dipole representations of V1 and V2 activations are shown on the reconstructed cortical surface. d) The first step in constructing the mffMRI grid is to connect the mean locations of strongest activations representing the visual field regions in the same eccentricities and then e) connect them along equal polarity directions. f) The final grid after optimizing the distance between neighboring nodes in 2D and g) in 3D.*

a node to the neighboring nodes is more than the standard deviation of the overall mean distance between neighboring nodes, it is checked if there are other active clusters for that visual field representation which fit better in the grid. Here, it is assumed that the distances between neighboring nodes should be equal. This is a good approximation when the stimulated regions are scaled according to human cortical magnification. The standard deviation and mean distance is recalculated every time the grid is modified.

Mainly because of the errors in segmentation of the anatomical data and in coregistration of functional and anatomical data, the similar thresholds in the localization of activations are not optimal to represent all the activations (see Fig. A.1a and

Fig. A.1b). The final step in constructing the mffMRI grid is to fit again the nodes whose mean distance to the neighboring nodes deviates from overall mean distance more than the standard deviation. This is implemented in *mffmri_grid.m* so that the T value threshold in activation localization is first elevated and then reduced together with the cluster size thresholds. In each step it is checked whether the new node locations make the grid more uniform. In Fig. A.1f is an example of the resulting grid and in Fig. A.1g the same grid in 3D model.

In some cases the grid algorithm does not result in the optimal grid and some manual corrections are needed. Because of imperfect coregistration of functional image to reconstructed cortex, an activation can for example be displaced across a sulcus and there are only a few active voxels in V1. The grid algorithm does not find this weak activation. In cases like this, it is possible to force the grid to go through some predefined node which is localized manually from the activation pattern.

A.2 3D Display for Multifocal Responses

The 3D display for multifocal responses *mffmri_display.m* is developed based on SPM2 function *spm_image.m*. It calls the SPM2 functions *spm_getSPM.m* and *spm_orthviews.m*. With *mffmri_display.m* the active voxels corresponding the stimulation of one hemifield or all the 60 visual field regions can be added as blobs to the structural image. The user can select what kind of statistical corrections (*none*, *FWE*, *FDR*) and thresholds (p value and cluster size) are used. The number of active clusters per visual field region can also be delimited. With the present multifocal stimulus the statistically most significant responses are almost always in V1. When the cluster number is limited to one cluster per visual field region, responses in V1 are visualized. The maximum number of voxels per cluster can also be limited. This is useful when a cluster representing one visual field area is several times larger than the other visual field representations. It is possible to choose whether the colors of the clusters code the eccentricity or the polar angle of the visual field. The clusters can also be equal colored for the visual area localization purposes. When the clusters are added in the anatomical image the simple user interface of *mffmri_display.m* enables user to go through the locations of the maximum T values in clusters with push buttons.

A.3 Estimation of Parameters in Log Polar Map Model of Visual Field Representation in Visual Cortex

As stated in chapter 2.4 the visual field representation in the visual cortex can be modeled with a conformal mapping technique. Visual field (z) is projected to the unfolded visual cortex

$$w = k \cdot \ln(z + a), \quad (\text{A.1})$$

where w (point in flattened cortex) and z (point in visual field) are complex numbers and parameters a and k scalars. Function *mffmri_logmapvf.m* is implemented to study how well this log polar map of the visual field representation in cortex fits to the multifocal activation patterns. With this function the best fitting parameters a and k are searched. The mean V1 locations of the multifocal activations are taken from mffMRI grids.

The best fitting parameters a and k are obtained using a nonlinear optimization technique in Matlab (*lsqnonlin.m*). The complex numbers are temporarily decomposed into real and imaginary parts to optimize the scalar constants. An additional parameter b is added to scale the width of the map [26]. The starting values ($a = 0.7$ $k = 17$) in the optimization as well as the boundaries ($a \in [0.001 \dots 3]$, $k \in [-30 \dots 30]$) are chosen based on previous studies [26].

To find the best fit, the model points need to be rotated and translated into the same space with the mffMRI grid. Let p_i^{data} be the nodes in the mffMRI grid and p_i^{model} the locations of the log-polar model points. Then, the error term to be minimized is

$$error = \sum_{i=1}^N |p_i^{data} - (Rp_i^{model} + T)|^2, \quad (\text{A.2})$$

where R is a rotation matrix and T a translation vector.

To determine R and T , the mean locations of the set of points (a^{data}, a^{model}) are first calculated. The new origins for the set of points are $n_i^{data} = p_i^{data} - a^{data}$ and $n_i^{model} = p_i^{model} - a^{model}$. The covariance matrix is $X = \sum_{i=1}^N n_i^{model} n_i^{dataT}$. From the singular value decomposition

$$[USV] = svd(X), \quad (A.3)$$

the rotation matrix is

$$R = VU^T \quad (A.4)$$

and then the translation vector is

$$T = a^{data} - Ra^{model}. \quad (A.5)$$

Then the nodes of the model grid are

$$w_i^{model} = R \cdot_i^{model} + T \quad (A.6)$$

The root mean square (RMS) error E_{RMS} is

$$E_{RMS} = \sqrt{\frac{\sum_{i=1}^N (p_i^{data} - w_i^{model})^2}{N}}, \quad (A.7)$$

where N is the number of nodes. [66]

In Fig. A.2 is illustrated how visual field mesh corresponding to mean locations of the multifocal stimulus in one hemifield is first projected to the unfolded cortical surface using the starting values and then, after optimization of parameters a and k and the position of the grid, how well the model grid fits to the mffMRI grid.

In *mffmri_logmapvf.m* it is also possible to exclude some nodes from the mffMRI grid from the optimization. This is recommended, when there are outliers in the mffMRI grid that trouble the registration of the model grid to the mffMRI grid.

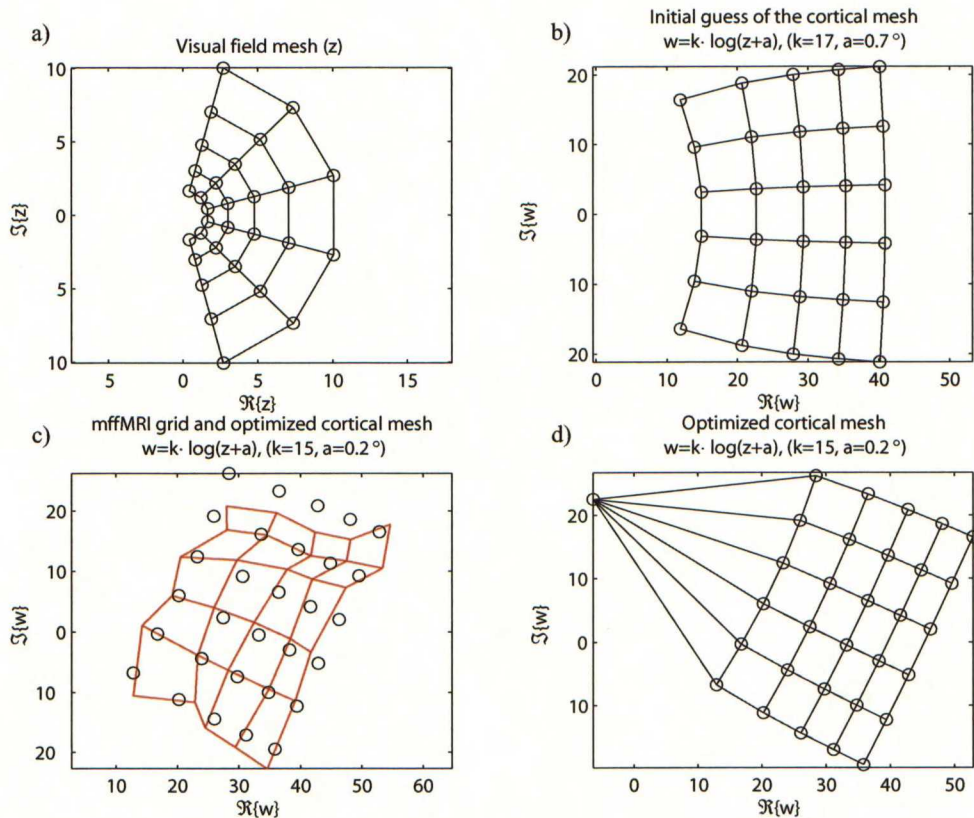


Figure A.2: a) The nodes of the visual field mesh correspond to the mean locations of the visual field regions in the multifocal stimulus. b) As starting values in the projection of the visual field mesh to a mesh in the cortical mesh $a=0.7^\circ$ and $k=17$ are used. The a represents the cortical surface devoted to foveal region. c) As an example one mffMRI grid and the optimized model grid are shown and d) the same model grid where the origin is also modeled to highlight the cortical surface devoted to small eccentricities.